

Article

Major and Trace-Element Composition of Minerals in the Paleoproterozoic Tikshezero Ultramafic–Alkaline–Carbonatite Complex, Russia: Insight into Magma Evolution

Maria Bogina *, Alexey Chistyakov, Evgenii Sharkov, Elena Kovalchuk and Tatiana Golovanova

Institute of Geology of Ore Deposits Petrography Mineralogy and Geochemistry, Russian Academy of Sciences, Staromonetny per., 35, 119017 Moscow, Russia

* Correspondence: lekhta@mail.ru; Tel.: +7-905-558-6928

Abstract: The Middle Paleoproterozoic (1.99 Ga) Tikshezero ultramafic-alkaline-carbonatite complex in Northern Karelia is one of the Earth's oldest alkaline complexes. The major and trace-element compositions of minerals were used to decipher the genetic relations between ultramafic cumulates, alkaline rocks, and carbonatites. Based on detailed analysis of clinopyroxenes from ultramafic cumulates, it was assumed that they were derived from an alkaline melt. It was estimated that ultramafic cumulates and alkaline rocks were formed at close moderate pressure, which in combination with the above facts, is consistent with their cogenetic origin. The REE patterns of clinopyroxenes are characterized by the high LREE/HREE fractionation, with slightly convex-upward LREE patterns ($La/Nd < 1$), which are typical of deep-seated cumulates formed in an equilibrium with an alkaline basaltic melt. Two types of REE zoning were distinguished in apatite using cathodoluminescence imaging. The first type with an outward LREE decrease was found in apatite from silicate rocks of the complex and was likely produced by the closed-system overgrowth of apatite from a residual melt at the late magmatic stage. In contrast, apatite from carbonatite is characterized by a slight outward LREE increase, which is likely related to the re-equilibration of apatite with fresh batches of REE-enriched carbonatite magma. Precipitation of monazite along fractures and margins of apatite in complex with essential HREE and Y enrichment observed in syenite is indicative of the metasomatic interaction of this rock with fluid. Apatites from alkaline rocks and carbonatites define a common trend in the Y–Ho diagram, with a decrease in the Y/Ho ratio from foidolites to carbonatites. This fact together with the absence of signs of liquid immiscibility, and compositional variations in apatite in silicate rocks and carbonatites, are consistent with their origin through fractional crystallization rather than liquid immiscibility.

Keywords: ultramafic–alkaline–carbonatite complex; Karelian craton; fractional crystallization; liquid immiscibility; cathodoluminescence imaging; apatites; clinopyroxene; trace-element composition



Citation: Bogina, M.; Chistyakov, A.; Sharkov, E.; Kovalchuk, E.; Golovanova, T. Major and Trace-Element Composition of Minerals in the Paleoproterozoic Tikshezero Ultramafic–Alkaline–Carbonatite Complex, Russia: Insight into Magma Evolution. *Minerals* **2023**, *13*, 1318. <https://doi.org/10.3390/min13101318>

Academic Editor: Anastassia Yurievna Borisova

Received: 3 September 2023

Revised: 6 October 2023

Accepted: 10 October 2023

Published: 11 October 2023



Copyright: © 2023 by the authors. Licensee MDPI, Basel, Switzerland. This article is an open access article distributed under the terms and conditions of the Creative Commons Attribution (CC BY) license (<https://creativecommons.org/licenses/by/4.0/>).

1. Introduction

The evolution of magma composition strongly depends on processes proceeding in magmatic chambers such as magma mixing crystallization, assimilation, as well late magmatic–hydrothermal and metasomatic alterations related to the influence of internal or external fluids. Of great significance in this respect is the study of exhumed magma reservoirs (intrusions), which provide deeper insight into understanding the above-mentioned magmatic processes [1]. Minerals are sensitive indicators of change in magmatic environments and conserve information on the history of magmatic processes. Their study in these plutonic systems is an efficient petrogenetic tool for deciphering magmatic evolution. Analysis of these minerals from different phases and rocks of the massif highlights the magmatic evolution from early to late magmatic stages and the contribution of other sources, for instance, fluids, to their formation. In this work, we analyzed the composition of minerals from the Tikshezero complex. The Tikshezero ultramafic–alkaline complex

with carbonatites is one of the Earth's oldest alkaline complexes (1.99 Ga) and represents the oldest massif consisting of a complete spectrum of low-alkali ultramafic–mafic rocks (dunites, clinopyroxenites, gabbro) and silica-undersaturated alkaline rocks (jacupirangite, melteigite, ijolite, urtite, theralite, and syenite) in association with carbonatites. The previous studies of this complex have been mainly focused on the geochronological dating and isotope-geochemical analysis of carbonatites, whereas silicate rocks that compose most parts of the complex remained poorly studied [2–4]. Our recent studies [5,6] were dedicated to the detailed petrographic, mineralogical, and chemical examination of all rock varieties and included microprobe study of minerals, as well as the petro- and geochemical and isotope-geochemical (Sr-Nd-Hf-Pb-Os) study of all rocks.

The obtained data allowed us to shed light on the petrology of the complex, some genetic aspects of the relations between the alkaline silicate phases of the complex, and to propose a genetic model of their formation [5]. Two alternative models of the formation of the low-alkali ultramafic–mafic and alkaline phases of the massif were proposed: (1) from a single mantle source through successive two-stage melting and (2) three-stage model related to the ascent and melting of the mantle plume [6]. However, relations of the silicate and carbonatite phases, origin of carbonatites, as well as their evolution, remained beyond the scope of these works. In addition, many questions regarding the genetic relationship of the ultramafic part of the massif with alkaline magmas remained incompletely solved. In this work, these problems are discussed using first obtained in situ LA-ICP-MS data on minerals from all intrusive phases of the Tikshezero complex in combination with previously obtained microprobe and geochemical studies ([5,6]).

2. Geology

The Tikshezero ultramafic–alkaline complex with carbonatites is located in the eastern Fennoscandian shield and has an age of ~1.99 Ga based on U-Pb zircon dating of carbonatites [2–4]. The complex intrudes the Archean granite gneisses and Paleoproterozoic granites (Figure 1).

It is a central-type concentrically zoned multi-phase intrusion 24 km² in area. The complex is split by faults into several blocks: Central, Shapkozero, and Tikshezero (Figure 1), which were described in detail in [5]. Three intrusive phases are distinguished: (1) low-alkali ultramafic rocks (dunites, wehrlites, clinopyroxenites, and gabbro); (2) alkaline rocks subdivided into foidolites (alkaline clinopyroxenites, jacupirangites, ijolites, melteigites, urtites) and a group of nepheline syenites and theralites; (3) calcite carbonatites and associated carbonate–silicate rocks. Ultramafic–mafic rocks (phase 1) compose the western Shapkozero block, whereas the Central and Tikshezero blocks are made up of alkaline rocks of the second phase. Carbonatites (phase 3) occur as stockwork bodies in the central part of the intrusion, mainly at the block contacts (Figure 1). Due to the poor exposure, the direct relationships between ultramafic and alkaline rocks are unknown, whereas carbonatites intrude both phases and contain their fragments in contact breccias. Carbonate–silicate rocks are developed at the contact between carbonatites and silicate rocks along the perimeter of carbonatite bodies and likely represent products of metasomatic transformations of silicate rocks due to the carbonatite emplacement. They are usually made up of fine-grained aggregates of silicate minerals (mainly alkaline amphibole and biotite), among large carbonate grains, that compose less than half of the volume (Table 1). Thereby, the quantitative relations of silicate minerals and carbonates could significantly vary. The rocks experienced a subtle greenschist alteration expressed in the partial serpentinization of olivine, as well as the replacement of primary clinopyroxenes and pargasite–kaersutite amphiboles by secondary fibrous actinolite. Analysis of the trace-element composition of minerals was carried out for unaltered or weakly altered rocks.

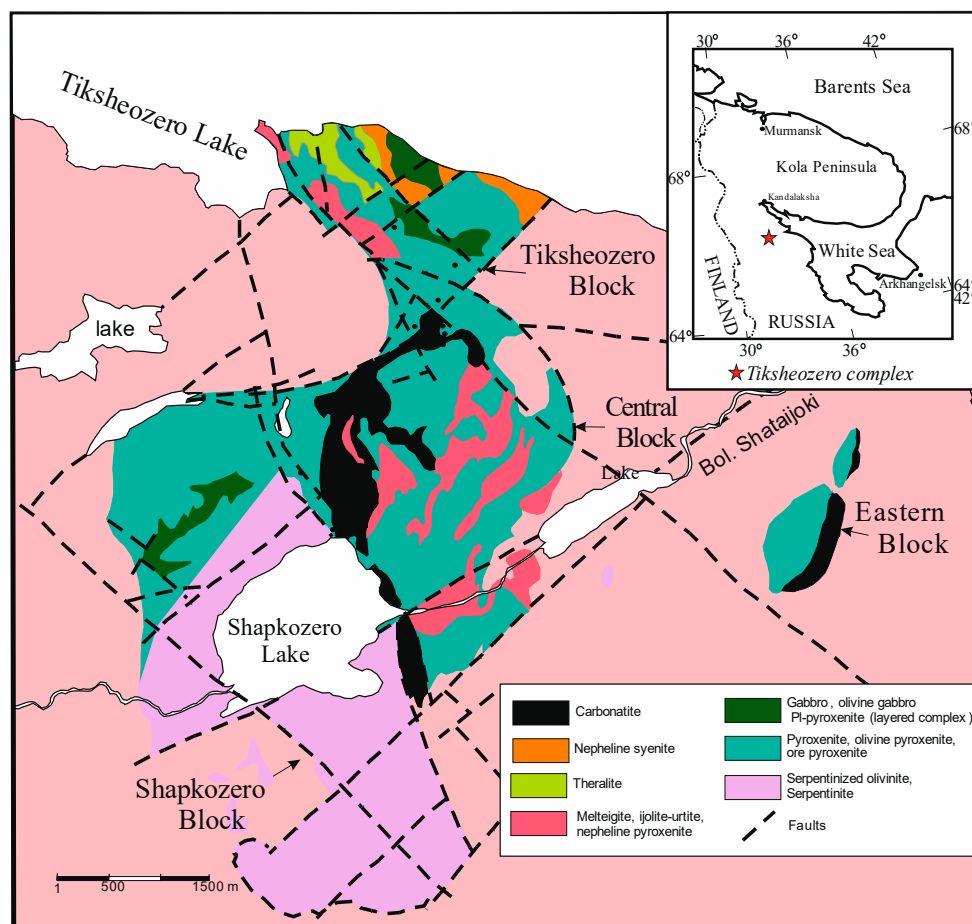


Figure 1. Geological scheme of the Tikshezero complex (modified after [7]). Inset indicates its geographical position.

Table 1. Petrography of studied rocks.

Sample No., Rock	Brief Characteristics
T2 Ol+Cpx cumulate (wehrlite)	Medium-grained rock. Olivine (60–70 vol %) and Cpx form anhedral grains up to 5–6 mm. Single small Fe-Ti oxides and sulfides (pentlandite). Secondary minerals are serpentine and actinolite.
T4 Ol clinopyroxenite	Scarce olivine grains of irregular shape form aggregates (2–6 mm) among Cpx (up to 5 mm). Single small Fe-Ti oxides and calcite veinlets.
T18 Ol clinopyroxenite	Massive rock. Cpx (>80%, up to 5 mm). Scarce Ol—grains of irregular shape up to 2–3 mm in size. Accessory small Fe-Ti oxides. Secondary minerals: serpentine and actinolite.
T22 Ol gabbro	Ol (10 vol %) and Cpx (70 vol %) form grains of irregular shape from 0.2 to 6–7 mm. Pl forms aggregates of small grains. Fe-Ti (up to 5 vol %)—small inclusions, mainly in Cpx.
21–35 Alkaline clinopyroxenite	Fine to medium-grained inequigranular rock. Composition: Cpx (~20 vol %, up to 1 mm), Ferro-Krs (30–40 vol %, up to 3–4 mm), interstitial Pl, small Fe-Ti oxides (up to 5%), accessory F-Ap.
T15 Jacupirangite	Fine to medium-grained inequigranular rock. Composition: Cpx (70 vol %, from 0.1 to 3 mm), interstitial Ne (~10 vol %), small Fe-Ti oxides (10 vol%), Krs—grains up to 1–2 mm and oikocrysts with inclusions of Cpx and Fe-Ti.
834 Jacupirangite	Fine to medium-grained inequigranular rock. Composition: Cpx Ti-augite (subhedral grains ~ 50 vol %, size from 0.1 to 2 mm), Krs (30–40 vol %, oikocrysts up to 3–4 mm, with inclusions Cpx and single Ol), small interstitial Ne (up to 5 vol %), Fe-Ti oxides (3–5 vol %, up to 0.5 mm), single Phl and accessory F-Ap.
T32 Melteigite-ijolite	Fine to medium-grained inequigranular rock. Composition: Cpx (Ti-augite, up to 2–3 mm), Krs (up to 1 cm, frequently oikocrysts) and Ne (small interstices and large oikocrysts) approximately in equal amounts compose almost whole rock volume. Chadacrysts—Cpx. Single small Fe-Ti oxides, accessory F-Ap.

Table 1. Cont.

Sample No., Rock	Brief Characteristics
32-1 Melteigite	Fine to medium-grained rock. Cpx (35 vol%)–Ti-augite, Ne (30–35 vol %), Fe-Ti oxides (up to 10 vol %), phlogopite (up to 20 vol%), single grains of calcite, accessory: F-Ap, Spn, Prv.
32-2 Melteigite–ijolite	Fine to medium-grained inequigranular rock. Cpx and Ne amount 80 vol %, show uneven distribution. Cpx forms accumulations (up to 8 mm) of subhedral grains with interstitial Ne and grains up to 3–4 mm in size among finer-grained (1–2 mm) Ne grains. Bt forms grains or intergrowths with Fe-Ti oxides. Accessory: F-Ap and Spn, Cal veinlets.
T32a Theralite	Fine to medium-grained inequigranular rock. Composition: Ti-Aug (40–50 vol %, up to 1 mm) and Pl (20 vol %) form accumulations of small grains; small Fe-Ti oxides (up to 10 vol %) with single Bt; other minerals—Ne (up to 2–3 mm); accessory –F-Ap.
26-7 Theralite	Medium-grained rock consisting of Cpx (40 vol %, 0.1 to 1.5–2 mm), Pl (0.2 to 3 mm) and Ne (frequently > 3 mm) approximately in equal amounts—up to 50 vol %; Bt and Fe-Ti oxides, frequently with small F-Ap inclusions.
T46 Syenite	Massive medium-grained leucocratic rock. Composition: Kfs (~60 vol %, frequently > 6 mm); Ne (~20 vol %, 2–6 mm); fine to medium-grained Kfs between large grains, mafic minerals (up to 20 vol %, up to 2–3 mm)—accumulations of pargasitic amphibole, accessory F-Ap.
835 Carb–Sil rock	“Patchy” rock. Mafic patches (3–7 mm) are composed of fine-grained aggregate of mainly alkaline Amp with Bt; leucocratic patches—Cal, or fine-grained cancrinite-albite-sodalite composition. Accessory F-Ap.
839 Carb–Sil rock	“Patchy” rock. Composition: alkaline Amp and Aeg (mafic “spots”); carbonate (grains up to 2–3 mm, veinlets and leucocratic “spots”); small (a few tenths of mm) and large (up to 2–3 mm) grains of Fe-apatite; Ilm—single small grains or their accumulations; accessory titanite.
37-9 Carb–Sil rock	Clusters of fine-grained Phl and alkaline amphibole account for up to half of rock volume, remaining volume is occupied by calcite grains, single Fe-Ti oxides, accessory F-Ap.
169/200 154/133 154/99 Carbonatite	Fine to medium-grained inequigranular rock. Anhedral calcites compose up to 80 vol %. ~10% are grains of F-apatite from a tenth of mm to 0.5 mm in size that occur as inclusions in calcite and in interstices between carbonate grains. Remaining volume is occupied by magnetite (up to 0.5 mm) and phlogopite, amphibole (richterite-cataphorite) and F-Ap, which sometimes form clusters surrounded by Fe-Mg carbonate—dolomite.

Abbreviations: minerals: (Ol) olivine, (Cpx) clinopyroxene, (Pl) plagioclase, (F-Ap) fluorapatite, (Amp) amphibole, (Aeg) aegirine, (Ne) nepheline, (Kfs) K-Feldspar, (Krs) kaersutite, (Phl) phlogopite, (Ilm) ilmenite, (Cal) calcite. Rocks: (Carb–Sil rock) carbonate–silicate rock.

3. Materials and Methods

Clinopyroxene, apatite, amphibole, and carbonates were studied in clinopyroxenites and gabbro (T2, T18, T4, T22), alkaline clinopyroxenite (21/35), jacupirangite (T15, 834), ijolite–melteigite (T32, 32-2, 32-1), theralite (T32a, 26-7), syenite (T 46, 27-15), in carbonate–silicate rocks (839, 37-9, 835), and carbonatites (154/133, 154/99, 169/200). Petrographic characteristics of the studied rocks are listed in the table below. Major element compositions of the studied minerals, except for apatite zoning, are reported in [5]. The petrography of the studied samples is given in Table 1 and shown in Figure 2.

The trace-element composition of apatite, clinopyroxene, amphibole, and carbonate was analyzed via LA-ICP-MS on an X-Series II coupled with NWR-213 laser ablation sampler at the Laboratory of Mineral Analysis of the Institute of Geology of Ore Deposits, Petrography, Mineralogy, and Geochemistry Russian Academy of Sciences (IGEM RAS). A sample was introduced in mass spectrometer as aerosol with Ar flow, ionized in inductively coupled plasma, and then, separated using quadrupole mass analyzer. Secondary ions were detected by an electron multiplier that preserved linearity within a range of 1 to 10¹⁰ ions per second. Ablation conditions were as follows: laser pulse energy 18–19 J, pulse frequency of 10 Hz, ablation crater of 60 µm in diameter, and ablation time of 30 s.

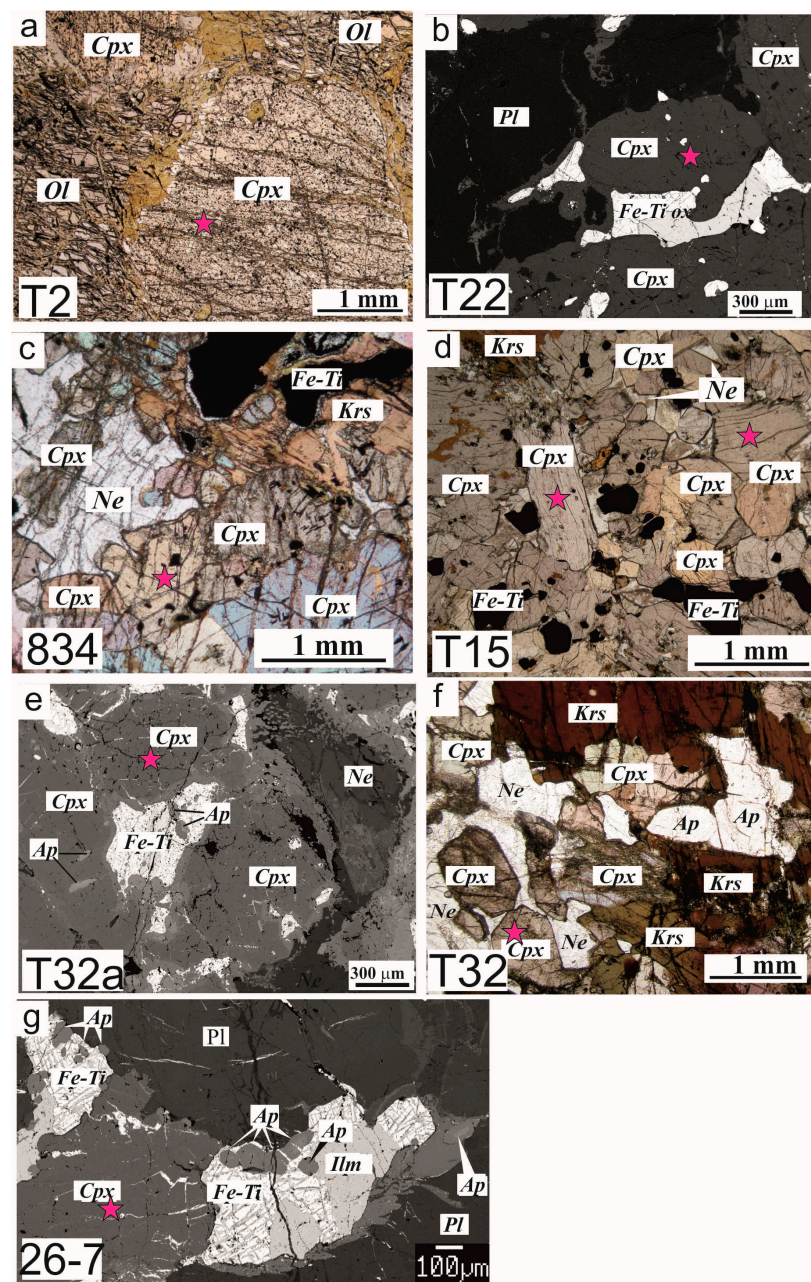


Figure 2. Microphotographs ((a,c,d,f), parallel nicols) and BSE images (b,e,g) of the studied rocks of the Tikshezzero complex. Asterisks show analyzed spots. Mineral abbreviations: (Ol) olivine, (Cpx) clinopyroxene, (Pl) plagioclase, (Ap) apatite, (Ne) nepheline, (Kfs) K-Feldspar, (Krs) kaersutite, (Fe-Ti) Fe-Ti oxides, and (Ilm) ilmenite.

The intensity of the laser ablation signal was calibrated using NIST SRM 612 glass reference material. The measurement errors were 1%–3% for REE, U, Th, Pb and 30%–50% for Ni, Cu, Zn, Co. Concentrations of elements were calculated using glass reference materials with known element concentrations (NIST SRM 610 and NIST SRM 612), the matrix composition of which is close to that of the analyzed phases. Analyses were carried out in polished thin sections on epoxy resin or in epoxy-mounted individual mineral grains.

Zoning of apatite was analyzed via electron-probe microanalysis (EPMA) using a JEOL JXA-8200 equipped with five wavelength spectrometers at the Institute of Geology of Ore Deposits, Petrography, Mineralogy and Geochemistry, Russian Academy of Sciences (IGEM RAS), Moscow, Russia. Operation conditions were as follows: accelerating beam voltage of 20 kV, a beam current of 20 nA, a beam diameter of 1–2 μm, and a 10 s counting

time at peak positions for major elements and 20–40 s for trace elements. The instrument was calibrated daily using both natural and synthetic reference material, and measurements were corrected with the JEOL ZAF routine.

Color cathodoluminescence images of apatite were obtained using the MS-46 micro-analyzer (Cameca, Gennevilliers, France) supplemented by an original optical detector adapted from the Videoscanner-285 high-resolution camera (Videoscanner, Russian Federation) and USB 2000 + VIS-NIR-ES spectrometer (Ocean OpticsUSA). Unlike the serial manufactured detectors, this technique provides true color cathodoluminescence images. For CL registration, the beam was scanned in a raster mode at an accelerating voltage of 20 kV, beam current of 20 nA, and exposure time of 239.7 s.

4. Results

4.1. Clinopyroxene

Clinopyroxene is present in practically all rocks of the complex, except for carbonatites. The characteristic feature of the studied pyroxenes is their homogenous composition within a grain.

In the low-alkali ultramafic rocks of the first intrusive phase, clinopyroxene is the major mineral in wehrlites, olivine clinopyroxenites, clinopyroxenites, and gabbro (Figure 2a,b). In wehrlites, clinopyroxene ($Wo_{46-48}En_{44-46}Fs_{7-8}$) together with olivine forms independent granular grains resembling cumulus phases up to 5–6 mm in size (Figure 2a, sample T2). In olivine clinopyroxenites and clinopyroxenites (sample T4 and T18), clinopyroxene ($Wo_{43-47}En_{44-49}Fs_{7-10}$) represents the main cumulus phase and forms intergrowths of grains from 0.1 to 4–5 mm of different morphology, forming an adcumulate texture. In *Ol* ferrogabbro (sample T22) that composes the upper part of the preserved Shapkozero block, clinopyroxene ($Wo_{47}En_{41}Fs_{12}$) also forms intergrowths with olivine and Fe-Ti oxides, and frequently contains subhedral inclusions of the latter (Figure 2b).

Foidolites. In jacupirangites (samples T15 and 834), clinopyroxene ($Wo_{51-52}En_{33-35}Fs_{14-16}$) composes most parts of the rock; grains have subhedral or anhedral morphology from a few tenths of mm to 2–3 mm, with pink pleochroism. It forms clusters with small interstices filled with nepheline and as chadacrysts in large kaersutite oikokrysts (Figure 2c,d). In composition, *Cpx* corresponds to fassaite (Ti diopside with 3 wt % TiO_2 and 0.67–1.85 wt % Na_2O). In the melteigites and ijolites (samples T32, 32-2, and 32-1), clinopyroxene is Ti-augite ($Wo_{52-56}En_{36-37}Fs_{7-11}$) with pink pleochroism. It shows uneven distribution, forming clusters over 8 mm in size and large grains up to 3–4 mm embedded in nepheline groundmass, as well as contains inclusions of Phl and Fe-Ti oxides (Figure 2f).

In the theralites, clinopyroxene is also represented by Ti-augite ($Wo_{49}En_{26-29}Fs_{22-25}$ in sample 26-7 and $Wo_{52}En_{32}Fs_{16}$ in sample T32a). It occurs as single subhedral grains and clusters of small (1–1.5 mm) subhedral and anhedral grains, which frequently contain inclusions of apatite and Fe-Ti oxides (Figure 2e,g).

Carbonatites and carbonate–silicate rocks. In carbonatite, we found only one clinopyroxene grain, which in composition, corresponds to those of foidolites and likely was entrained during the ascent of carbonatite magma. The absence of clinopyroxenes in carbonatites could be related to the fact that this mineral becomes instable in the evolved carbonatite system and is replaced by phlogopite or amphibole [8]. In the carbonate–silicate rocks (sample 839), clinopyroxene is represented by aegirine, which is unevenly distributed over the rock as relatively large grains up to 1.5 mm in size and clusters of fine-grained aggregates with phlogopite, amphibole, calcite, and Fe-Ti oxides. The clinopyroxene grains in all phases show no zoning or compositional heterogeneity.

According to IMA classification, clinopyroxenes in ultramafic–mafic rocks, foidolites, theralites, and syenites correspond to diopsides [9].

Clinopyroxenes from the **low-alkali ultramafic–mafic series** are characterized by a high Mg composition with extremely high Cr contents (up to 4100 ppm) and high SiO_2 content (up to 52.50%) with low contents of Al_2O_3 (2.18%–3.86%) and TiO_2 (0.53%–1.26%).

The spidergrams show weak negative anomalies of Ti, Zr, Sr, and Nb. The clinopyroxenes are also depleted in Hf and Ta (Figure 3a). The REE patterns (Figure 3b) are characterized by the LREE enrichment relative to HREE ((La/Yb)_n = 2.2–4.1), (La/Sm = 0.69–1.49). The LREE patterns frequently have a convex-upward shape with La, Ce, and Pr depletion relative to Nd ((La/Nd)_n = 0.61–0.97) and fractionated HREE patterns ((Gd/Yb)_n = 2.07–3.00) (Figure 3b). The total REE content varies from 27.65 to 49 ppm (Table 2).

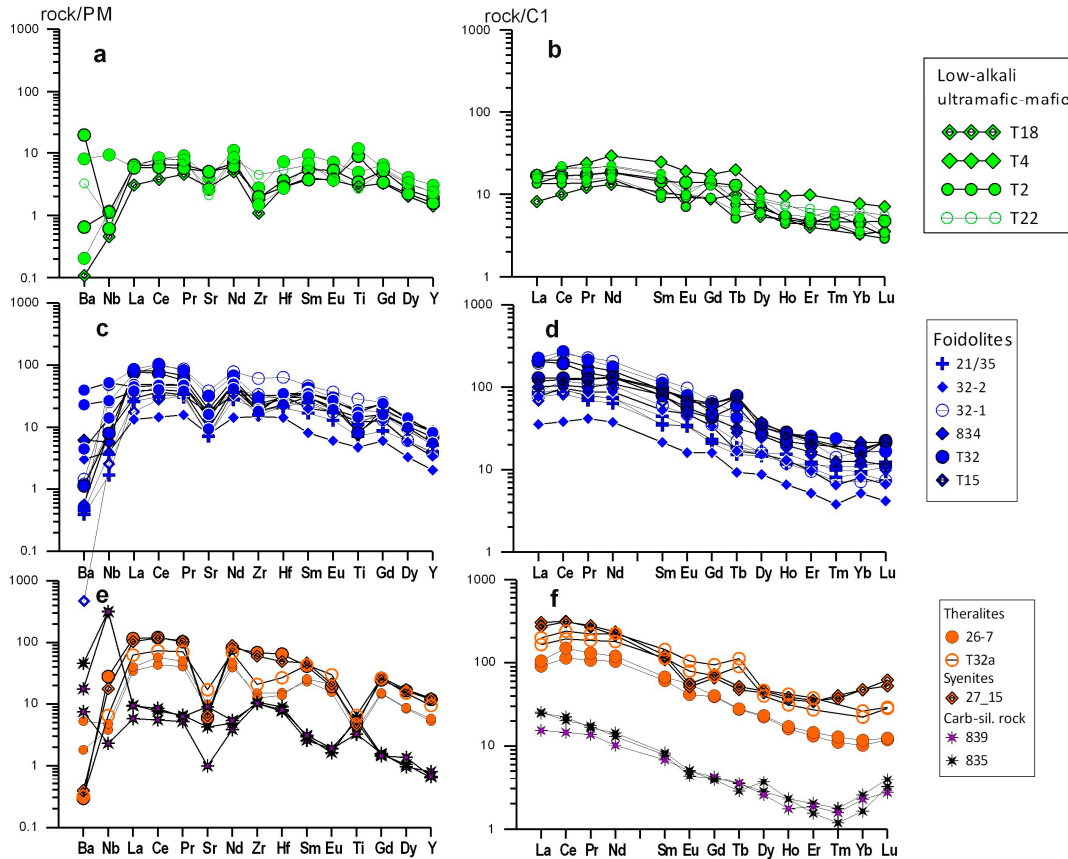


Figure 3. Trace-element and REE distribution patterns for clinopyroxenes of the Tiksheozero complex: (a,b) ultramafic–mafic rocks, (c,d) foidolites, (e,f) theralites, nephelibe syenites, and carbonate–silicate rocks. Concentrations are normalized to chondrite and primitive mantle after [10].

Table 2. Trace-element composition of clinopyroxene.

Sample	T2	T4	T18	T22	21/35	T15	834
Rock	Ol+Cpx Cumulates			Ol Gabbro	Alk. Cpyx	Jacupirangite	
Rb	2.39	0.71	2.20	0.18	1.51	2.04	0.16
Sr	51.7	100	75.5	70.0	50.0	40.1	41.7
Y	10.0	6.79	8.08	13.1	5.01	10.8	10.3
Zr	15.5	20.8	19.9	29.0	11.4	36.1	47.1
Nb	6.15	0.40	0.74	0.77	0.30	0.35	0.58
					1.66	1.44	1.11
					1.44	1.11	1.68
					2.40	17.5	3.78

Table 2. Cont.

Sample	T2	T4			T18	T22			21/35			T15		834	
Rock	Ol+Cpx Cumulates				Ol Gabbro				Alk. Cpyx			Jacupirangite			
Ba	53.2	128	4.28	1.35	0.71	15.1	21.5	2.5	2.82	2.58	0.10	3.00	151	40.8	
La	3.81	3.75	4.13	4.18	1.99	3.75	4.26	20.8	18.5	19.7	11.4	16.8	24.6	52.4	
Ce	14.1	9.87	10.7	13.4	6.34	11.9	12.8	60.6	53.3	58.9	46.9	52.0	67.1	135.4	
Pr	1.95	1.45	1.65	2.3	1.16	1.98	2.04	7.36	6.67	7.67	8.11	8.65	9.64	17.1	
Nd	10.5	7.60	8.68	13.8	6.24	10.8	10.2	35.5	30.2	34.6	44.9	45.2	52.1	74.7	
Sm	2.73	1.52	2.21	3.78	1.63	2.83	2.63	5.33	5.54	6.84	10.5	10.2	12.4	14.3	
Eu	0.57	0.59	0.81	1.10	0.56	0.84	0.65	1.96	1.95	1.99	2.96	2.63	2.96	4.33	
Gd	3.08	1.84	2.83	3.53	1.78	2.59	2.86	4.69	4.26	4.73	8.56	9.92	8.63	10.7	
Tb	0.32	0.24	0.48	0.74	0.37	0.46	0.33	0.69	0.57	0.66	1.03	1.05	1.18	2.81	
Dy	2.24	1.49	1.73	2.73	1.36	2.29	2.13	4.26	3.72	4.02	5.81	6.17	6.64	8.20	
Ho	0.32	0.27	0.30	0.54	0.28	0.43	0.41	0.66	0.70	0.87	1.04	1.05	1.12	1.54	
Er	0.89	0.80	0.78	1.63	0.66	0.98	1.11	1.94	1.73	2.04	2.49	2.51	2.70	4.25	
Tm	0.16	0.11				0.12	0.16	0.27	0.21	0.25	0.25	0.29	0.32		
Yb	0.86	0.59	0.76	1.27	0.54	1.01	1.02	1.82	1.47	1.56	1.92	1.91	2.08	3.52	
Lu	0.09	0.09	0.12	0.18	0.09	0.14	0.12	0.31	0.18	0.27	0.26	0.25	0.29	0.54	
Hf	0.77	0.81	1.02	2.05	0.81	1.28	1.51	5.94	5.89	5.75	6.45	6.06	6.53	8.12	
Ta	0.10	0.03	0.18	0.20	0.09	0.03	0.06	0.50	0.47	0.41	0.38	0.40	1.86	0.97	
Pb	3.30	6.59				1.16	1.51	0.36	0.39	0.24	0.05	0.78	3.30		
Th	0.50	0.30	0.24	0.06	0.03	0.46	0.66	0.51	0.37	0.54	0.14	0.96	1.81	5.81	
U	0.06	0.09	0.10	0.12	0.02	0.27	0.28	0.11	0.12	0.12	0.04	0.16	0.31	0.41	
Sample	T32	32-1			32-2		T32a		26-7		27-15		835	839	
Rock	Ijolite–Melteigite				Theralite				Syenite			Carb–Sil			
Rb			2.32	2.45	1.83	0.21			7.61	1.17	0.17	1.22	1.34	4.47	1.77
Sr	634	340	306	764	153	336	349	340	198	164	120	130	180	84.56	19.8
Y	35.1	29.63	16.3	36.5	8.73	14.6	50.1	40.8	25.0	22.9	51.1	53.3	2.88	2.76	3.44
Zr	313	250.6	352	640	155	340	302	219	131	157	718	628	108	112	107
Nb	31.9	5.22	6.22	16.9	2.64	5.50	7.77	4.31	3.15	2.51	18.4	11.69	207	210	1.52
Ba	3.41	7.46	7.97	9.60	20.0	3.88	6.75	2.05	34.9	12.0	1.92	2.54	117	302	49.6
La	55.2	50.6	21.7	47.6	8.64	18.8	48.8	40.5	25.8	22.3	74.9	66.8	6.06	6.22	3.77
Ce	173	123	76.0	163	24.3	1.00	153	123	95.9	72.7	201	198	14.2	12.9	9.28
Pr	20.6	14.4	10.6	22.0	4.00	8.36	21.4	18.0	12.6	10.4	26.0	27.0	1.59	1.68	1.32
Nd	83.9	62.5	49.8	97.6	17.9	41.6	107	85.4	57.0	49.2	101.7	111	6.80	6.15	4.82
Sm	17.3	12.2	9.12	18.8	3.29	8.08	22.3	17.5	10.4	9.41	16.73	19.0	1.27	1.20	1.05
Eu	4.59	3.27	2.70	5.67	0.93	2.74	6.08	4.61	3.22	2.42	2.97	3.26	0.29	0.25	0.29
Gd	9.62	8.80	7.14	13.7	3.27	6.87	19.4	14.3	8.21	8.01	13.44	14.7	0.78	0.83	0.86
Tb	1.59	2.24	0.83	1.81	0.35	0.63	4.21	3.38	1.05	1.04	1.78	1.94	0.11	0.13	0.13
Dy	8.51	6.99	4.10	8.48	2.21	3.90	11.8	10.1	5.88	5.68	11.09	11.6	0.92	0.71	0.65

Table 2. Cont.

Sample	T32	32-1		32-2		T32a		26-7		27-15		835		839	
Rock	Ijolite–Melteigite					Theralite				Syenite		Carb–Sil			
Ho	1.55	1.24	0.68	1.45	0.37	0.74	2.38	1.77	0.97	0.91	2.05	2.19	0.13	0.13	0.10
Er	4.24	3.34	1.57	3.55	0.86	1.59	6.28	4.51	2.41	2.19	5.64	5.87	0.26	0.33	0.31
Tm	0.61		0.18	0.36	0.10	0.17			0.33	0.28	1.04	0.95	0.03	0.05	0.04
Yb	2.69	2.98	1.17	2.70	0.85	1.31	4.35	3.67	1.93	1.68	7.82	7.84	0.27	0.42	0.37
Lu	0.42	0.54	0.19	0.43	0.11	0.17	0.74	0.72	0.31	0.30	1.58	1.34	0.08	0.10	0.07
Hf	8.40	8.49	8.10	18.0	4.04	9.16	11.5	7.58	3.93	4.33	18.4	13.9	2.28	2.60	2.18
Ta	3.10	0.92	1.65	2.93	0.58	1.39	1.49	1.28	0.48	0.47	2.57	2.12	1.89	1.98	0.12
Pb	1.31		0.62	1.58	3.85	0.30			0.52	0.90	0.91	0.29	4.15	3.36	3.72
Th	1.38	1.01	0.62	3.07	0.57	0.47	0.57	0.47	0.45	0.53	0.26	0.19	2.37	1.26	0.61
U	0.23	0.23	0.05	0.26	0.30	0.07	0.09	0.08	0.10	0.19	0.04	0.01	0.50	0.29	0.25

Notes: (Alk. Cpyx) alkaline clinopyroxenite, (carb–sil) carbonate–silicate rock.

In the rocks of the **foiolite series**, clinopyroxenes have the higher TiO₂ (1.55%–3.30%), Al₂O₃ (5.60–8.99), and elevated Na₂O (0.56–0.70) contents with lower contents of SiO₂ (44.80%–48.29%) compared to the low-alkali ultramafic series. In the spidergrams (Figure 3c), clinopyroxenes from rocks of the foiodolite series display a depletion in Ba and Nb with a shallow negative Sr anomaly and absent Ti anomaly. They demonstrate highly fractionated REE patterns ((La/Yb)_n = 7.7–13.8) with a weak to moderate LREE fractionation ((La/Sm)_n = 0.68–2.6), frequently with some depletion relative to Nd ((La/Nd)_n = 0.49–1.56), and moderate HREE fractionation ((Gd/Yb)_n = 2.38–4.92) with a total REE content from 146 to 384 ppm (Figure 3d). Clinopyroxenes in **theralite and nepheline syenite** are characterized by the intermediate parameters of most components between ultramafic rocks and foiodolites: TiO₂ (0.73%–1.88%) and Al₂O₃ (2.24–8.99 wt %), but have a higher Na₂O content (0.71–1.22) (Table 2).

The spidergrams demonstrate deep Sr and Ti anomalies with a depletion in Ba and Nb (Figure 3e). They have fractionated REE patterns ((La/Yb)_N = 5.74–9.00) with a close LREE fractionation (La/Sm)_N = 1.37–2.21, frequently with La depletion relative to Nd ((La/Nd)_N = 0.87–1.42). In the HREE region, the patterns of clinopyroxenes, especially from syenites, frequently have a convex-upward shape ((Gd/Yb)_N = 1.38–3.84) (Figure 3f). Syenites are peculiar in the higher HREE contents with a total REE from 186 to 472 ppm (Table 2).

Clinopyroxenes from **carbonate–silicate rock** differ sharply in composition from those described above. They have high Na₂O (up to 12.86%) and low CaO (4.26%–1.79%) contents. According to IMA classification, they correspond to aegirine [9]. They are enriched in Ba and Nb, have a varying Sr anomaly, a weakly expressed positive Zr–Hf anomaly, and Ti maximum (Figure 3e). The clinopyroxene is depleted in all REE relative to other clinopyroxenes. The REE patterns show a “concave” shape and HREE enrichment ((La/Yb)_n = 5.74–9.00, (La/Sm)_n = 1.37–2.81; (Gd/Yb)_n = 1.38–3.84) with lower total REE contents (from 23 to 32 ppm) (Figure 3f). Unlike other clinopyroxenes, they show no La depletion relative to Nd ((La/Nd) = 1.51–1.95) (Table 2).

4.2. Amphibole

Amphiboles are present in practically all rocks. Most amphiboles from silicate rocks are ascribed mainly to the pargasite–edenite series, except for jacupirangites where amphibole is represented by kaersutite (TiO₂—up to 5.47 wt %). Amphiboles in carbonate–silicate rocks correspond mainly to magnesio-cataphorite and that of carbonatites to richterite, according to [11]. The major element composition of amphibole was described in detail in [5].

In **ultramafic–mafic rocks**, it is developed after clinopyroxene. In **nepheline syenites**, amphibole forms clusters 2–3 mm in size among K-feldspar. In **foiodolites**, amphibole

occurs as large (up to 3–4 mm, in some rocks up to 1 cm) interstitial oikocrysts bearing chadacrysts of Cpx and Fe-Ti oxides.

In the **carbonatites**, amphibole occurs in fine-grained aggregates with Fe-Ti oxides and apatite, which are surrounded by carbonates. These aggregates are unevenly distributed, compose up to half of the rock volume or amphibole occurs as single grains up to 1 mm in size.

Amphibole from **foiidolites and syenites** is enriched in Sr and Y compared to carbonate-silicate rocks and carbonatites. In the trace-element patterns (Figure 4a), amphiboles from carbonatites are characterized by the positive Nb and Sr, Zr-Hf, and Ti anomalies and negative Eu anomaly. (Figure 4a). In contrast, amphibole silicate and carbonate-silicate rocks show practically no significant anomalies, except for very shallow Sr and Zr anomalies only in some samples (Figure 4a). Amphiboles in silicate rocks have a much higher total REE content (128–700 ppm) than amphibole from carbonate-silicate rocks (23–25 ppm) and carbonatites (0.42–5 ppm) (Figure 4b). Amphiboles from silicate rocks have a high REE fractionation at moderate-high LREE and HREE fractionation ((La/Yb)_n = 11.5–20.72, (La/Sm)_n = 1.38–4; (Gd/Yb)_n = 1.38–3.12). Amphiboles from carbonatites and calc-silicate rocks have a much lower REE fractionation at wide variations in the LREE and HREE fractionation ((La/Yb)_n = 5.14–14.17, (La/Sm)_n = 0.85–3.9; (Gd/Yb)_n = 1.38–11.08) (Table 3, Figure 4b).

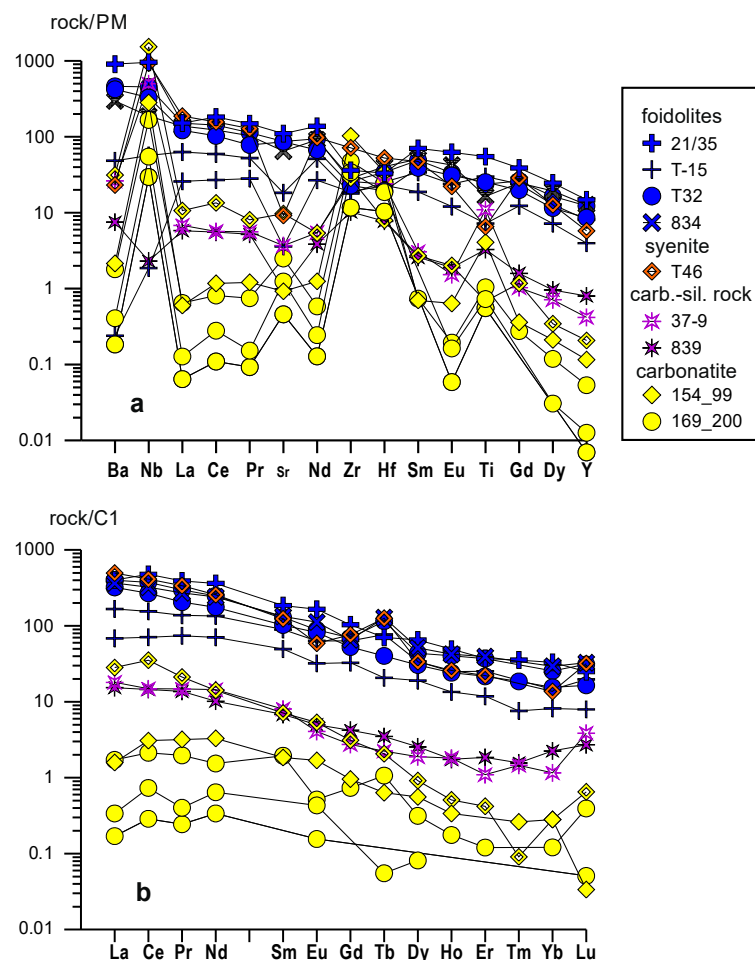


Figure 4. Trace-element (a) and REE (b) distribution patterns for amphiboles from the rocks of the Tikshezero complex. Concentrations are normalized to chondrite and primitive mantle after [10].

Table 3. Trace-element composition of amphiboles from the Tikshezero complex.

Sample	21/35	834	T15			T32		T46	154/99	169/200			154/133 37-9			839
Rock	Alk Cpyx	Jacupirangite			Melteigite–Ijolite		Syenite		Carbonatite			Carb–Sil				
Rb	15.9	bdl	10.5	0.08	11.2	13.4	7.35	27.2	0.48	0.4	0.2	0.43	0.34	3.4	6.54	1.77
Sr	2190	1289	363	71.4	777	1712	1726	183	18.4	24.7	29.2	9.13	49.6	193	73.3	19.8
Y	63.4	54.6	34.7	17.1	28.9	37.1	52.7	24.8	0.5	0.05	0.47	0.03	0.23	0.89	1.8	3.44
Zr	380	296	189	197	233	239	271	751	1078	359	310	122	496	298	271	107
Nb	630	123	37.3	1.23	128	216	298	615	185	36.1	24.2	19.4	110	1006	329	1.52
Ba	5980	1961	318	1.58	1518	2785	3048	153	14.2	2.69	11.3	1.22	11.9	206	173	49.6
La	98.2	89.8	40.9	16.8	61.7	78.6	97.8	121	0.39	0.08	0.37	0.04	0.42	6.9	4.41	3.77
Ce	305	206	99.1	45.2	135	171	239	263	1.97	0.47	1.17	0.18	1.36	22.5	9.48	9.28
Pr	37.7	26.3	13.3	7.13	16.5	19.8	28.8	32.6	0.31	0.04	0.15	0.02	0.19	2.05	1.42	1.32
Nd	172	114	63.9	33.4	68.0	83.5	117	121	1.56	0.31	0.42	0.16	0.73	6.72	6.84	4.82
Sm	28.6	20.6	13.8	7.63	13.1	15.8	20	19.1	0.28	bdl	0.10	bdl	0.30	1.10	1.24	1.05
Eu	9.62	6.51	3.68	1.86	3.54	4.76	5.13	3.42	0.10	0.03	0.03	0.01	0.03	0.31	0.24	0.29
Gd	21.2	13.4	13	6.68	10.1	10.8	14.2	15.6	0.2	bdl	0.18	bdl	0.15	0.64	0.56	0.86
Tb	2.65	4.82	2.88	0.77	1.24	1.51	4.32	4.72	0.02	bdl	bdl	bdl	0.04	0.08	0.08	0.13
Dy	16.6	13.0	8.64	4.84	7.22	7.76	11.1	8.56	0.14	0.02	0.03	bdl	0.08	0.23	0.48	0.65
Ho	2.80	2.40	1.42	0.76	1.21	1.37	2.29	1.47	0.02	bdl	bdl	bdl	0.01	0.03	0.10	0.10
Er	6.18	6.54	4.19	1.96	3.23	3.59	6.16	3.68	bdl	bdl	0	bdl	0.02	0.07	0.18	0.31
Tm	0.91			0.19	0.41	0.48			0.01	bdl	0	bdl		0	0.04	0.04
Yb	5.46	4.85	2.4	1.35	2.65	2.56	4.22	2.26	0.05	bdl	0.05	bdl	0.02	0.05	0.19	0.37
Lu	0.63	0.83	0.5	0.2	0.36	0.42	0.79	0.81		bdl	0.02	0	0.01	0.02	0.1	0.07
Hf	9.39	11.5	7.19	6.47	6.28	5.51	9.65	14.8	9.65	5.28	5.38	2.92	6.96	2.24	6.77	2.18
Ta	25.2	4.82	2.65	0.34	6.94	8.77	9.99	18.6	7.01	1.74	1.93	0.46	7.44	172	7.96	0.12
Pb	2.22			0.65	2.28	2.02			0.17	0.19	0.49	0.11		1.15	2.27	3.72
Th	1.16	1.95	2.72	1.47	0.79	1.17	0.99	0.01	0.04	0.01	0.04	0.01	0.32	20.7	2.43	0.61
U	0.38	0.35	0.37	0.17	0.16	0.18	0.16	0.01		0.10	1.19	bdl	10.3	136	0.30	0.25

Notes: (Alk. Cpyx) alkaline clinopyroxenite, (carb–sil) carbonate–silicate rock. Bdl—below detection limit.

4.3. Apatite

Apatites were studied using microprobe (Table S1) and LA-ICP-MS analyses (Table 4) and cathodoluminescence (CL) imaging (Figure 5 and Figure S1–S4).

4.3.1. Petrography

Apatite in **alkaline clinopyroxenite** (sample 21–35) in accessory amounts is unevenly distributed within the rock and occurs as small inclusions in clinopyroxene, plagioclase, and kaersutite. Apatite is represented by euhedral and subhedral short-prismatic grains up to 100 µm with an aspect ratio of 1:2. Sometimes, it forms larger grains with an aspect ratio of 1:5 and up to 500 µm long. In the cathodoluminescence (CL), apatite is light gray and shows no zoning.

Apatite in **ijolite–melteigites** (samples 32-1, 32-2, T32) is represented by single grains: (1) subhedral elongated grains forming inclusions in nepheline or in carbonate areas and/or (2) anhedral grains as inclusions in clinopyroxene and kaersutite. The size of the grains varies from a few tenths of microns to 1 mm. The largest size is typical of grains of the

second type. In CL, apatite crystals also have a violet-gray color, sometimes vague patchy, and lighter margins (Figure S1).

Theralites (T32a, 26-7) contain accessory subhedral, sometimes, bipyramidal and strongly elongated apatite grains as inclusions in mafic minerals (*Mgt*, *Cpx* and *Bt*) as well as scarce apatite aggregates. Sometimes, apatite grains are located at the contact of mafic minerals and feldspars. The grain size varies from a few microns to 0.15 mm. In CL, apatite shows clear zoning, with a violet or gray-violet core and light rim (Figure 5). In **syenites** (sample T46), accessory apatite forms elongated and equant, subhedral, and anhedral grains approximately from 10 to 100 μm , forming mainly inclusions in magnetite and intergrowths with mafic silicates. It demonstrates zoning observed both in the microprobe and in CL. In CL, apatite is turbid, has a dark-gray core and wide bluish-gray vaguely patched rim (Figure S2).

Table 4. Trace-element composition of apatite from the Tikshezero complex.

Sample	32-1	32-2	154/99		169/200			154/133		839	37-9	835		
Rock	Melteigite–Ijolite			Carbonatite						Carb–Sil				
Rb	170	3.08	2.56	0.01	0.00	0.02	bdl	bdl	bdl	bdl	33.7	30.40	2.80	3.09
Sr	486	36.43	32.9	6503	2577	5908	2471	6515	6487	7486	394	350	36.7	34.0
Y	19.8	4.09	3.60	40.15	3.15	25.3	2.93	56.2	32.8	40.9	42.9	40.7	4.65	3.95
Zr	353	28.89	26.6	bdl	0.05	bdl	bdl	0.09	bdl	bdl	297	281	32.9	26.3
Nb	4.70	0.55	0.50	bdl	0.44	bdl	bdl	0.05	bdl	bdl	4.97	4.60	0.54	0.49
Ba	1930	34.80	33.7	922	27.0	549	22.6	603	445	587	378	345	34.3	33.2
La	43.0	3.39	3.47	66.7	24.9	16.4	24.2	20.5	18.5	106	36.7	33.7	3.70	3.39
Ce	68.0	6.33	5.84	148	46.6	48.1	43.2	59.9	52.5	213	67.5	66.4	6.14	6.33
Pr	7.03	0.82	0.72	19.5	4.76	6.3	4.37	8.74	7.33	23.6	7.05	6.19	0.85	0.78
Nd	30.1	3.50	2.92	77.3	17.2	29.9	16.6	45.3	37.6	98.7	33.4	32.50	3.74	2.90
Sm	2.40	0.59	0.38	14.8	2.46	8.22	2.54	15.0	9.47	17.3	5.80	3.40	0.51	0.58
Eu	0.99	0.13	0.10	4.32	0.56	2.24	0.65	4.61	2.65	4.35	1.38	1.10	0.11	0.12
Gd	3.30	0.72	0.36	11.9	1.15	6.56	1.53	13.5	7.65	11.6	5.60	6.00	0.62	0.60
Tb	bdl	0.09	0.06	1.41	0.15	0.80	0.13	1.96	0.98	1.47	0.71	0.62	0.08	0.06
Dy	3.20	0.55	0.46	7.77	0.63	4.45	0.68	11.1	6.03	8.05	5.20	5.70	0.62	0.61
Ho	0.64	0.06	0.12	1.34	0.10	0.84	0.12	1.97	1.10	1.43	0.93	0.94	0.15	0.09
Er	1.42	0.35	0.28	3.40	0.18	2.18	0.31	4.86	2.94	3.90	2.32	2.95	0.31	0.41
Tm	0.18	0.04	0.03	0.37	0.03	0.31	0.02	0.72	0.41	0.52	0.46	0.34	0.05	0.05
Yb	2.20	0.30	0.23	2.53	0.12	1.82	0.10	3.52	2.61	2.78	2.17	1.64	0.38	0.31
Lu	0.12	0.05	0.02	0.33	0.02	0.28	0.03	0.55	0.38	0.46	0.51	0.62	0.03	0.05
Hf	7.90	0.73	0.66	bdl	bdl	bdl	bdl	bdl	bdl	bdl	6.30	6.20	0.78	0.63
Ta	0.60	0.04	0.04	bdl	0.03	bdl	bdl	bdl	bdl	bdl	0.39	0.51	0.05	0.06
Pb	36.6	6.26	5.77	3.02	1.22	1.16	1.41	1.50	0.74	2.99	67.0	67.8	5.79	6.52
Th	8.19	0.79	0.77	bdl	bdl	bdl	0.01	0.00	bdl	bdl	8.29	7.83	0.93	0.78
U	2.44	0.59	0.49	bdl	0.06	bdl	0.00	0.00	bdl	bdl	4.88	5.41	0.45	0.48

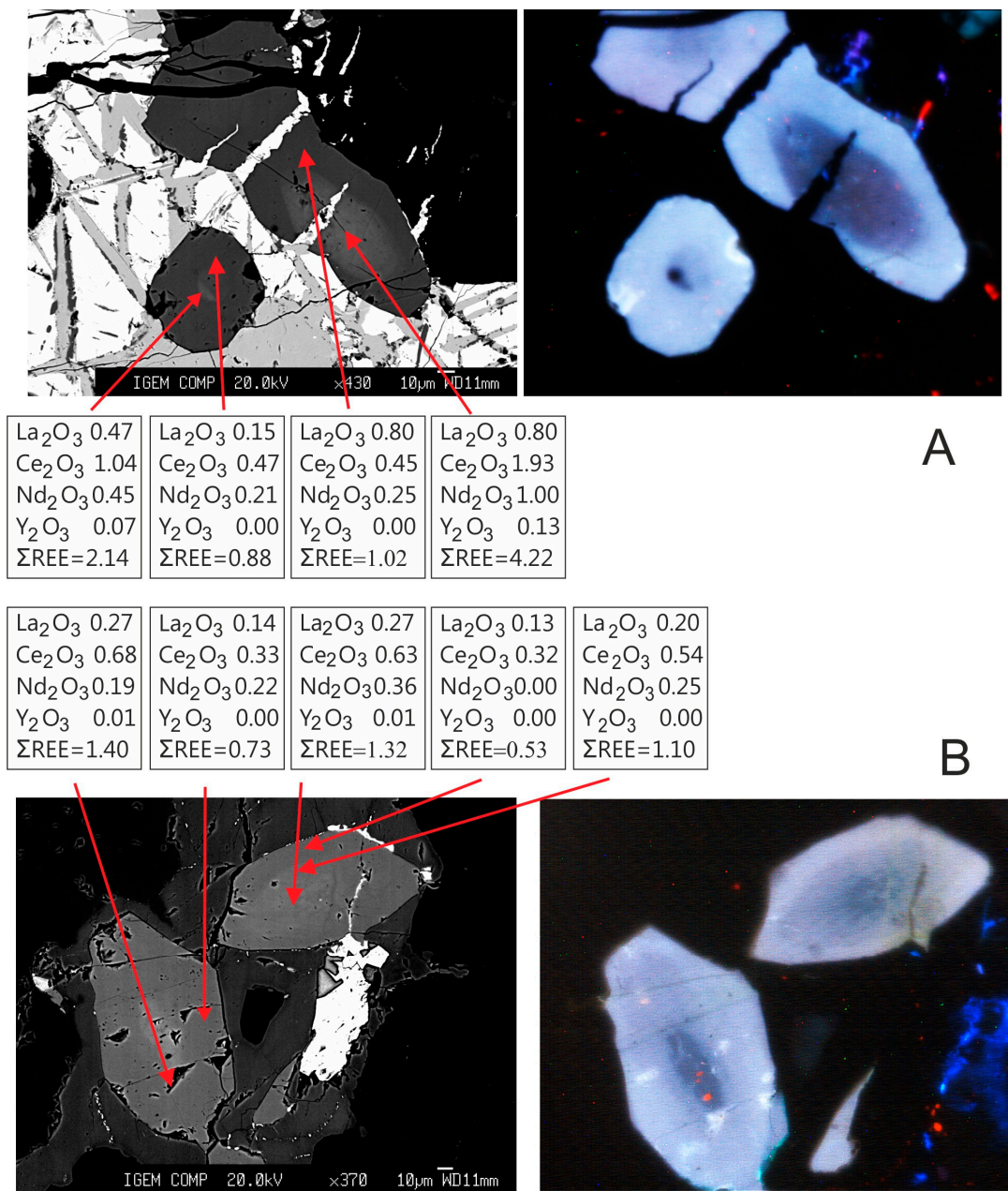


Figure 5. BSE and CL images of zoned apatites from theralite, samples 26-7 (A) and T32a (B).

In the **carbonate–silicate rocks** (samples 835, 839), apatite has the most complex structure, forming both euhedral up to 0.1 mm in size and large anhedral grains up to 1.5 mm with oscillatory zoning. The first type of apatites is mainly observed as embedded in a carbonate matrix, whereas the second type is confined to the contact of fine-grained accumulations of silicate minerals (amphibole and biotite) with carbonates. In CL, apatite is reddish-gray, sometimes with a lighter core (sample 835) and with numerous small rounded inclusions of carbonate (sample 369, Figure S3).

Carbonatites (samples 154/99, 154/133, 169/200) contain up to 15–20 vol % apatite. Thereby, cumulate apatite is developed mainly among carbonate, forming crystals of diverse morphology: from subhedral prismatic to anhedral grains. The grain size varies from a few tenths of mm to 2 mm. Apatite observed among accumulations of mafic minerals (phlogopite, amphibole, and ilmenite–magnetite) has a complex shape. In CL, apatite is gray, vaguely patched (Figure S4).

4.3.2. Chemistry

Apatite in the studied rocks has a narrow range of CaO from 53.44 to 55.57 and wide variations in P₂O₅ contents (40.59–43.59 wt %), which indicate the wide substitution in the P site. The mineral corresponds to F-apatite with wide F variations from 1.61 to 3.72 wt %, which is lower than the formula maximum of 3.73 wt %. The highest F content was found in alkaline clinopyroxenites and successively decreased to carbonatites. Carbonate–silicate rocks have an intermediate F content between syenites and carbonatites (2.19–2.39 wt %). The Cl content is close to the detection limit. MgO contents are mainly below the detection limits. The SrO content varies from 0.09 to 0.55, reaching maximum contents in carbonatites.

Primitive mantle-normalized patterns (Figure 6a,c) of alkaline rocks and carbonatites have a similar shape with negative anomalies of Nb, Zr-Hf, and Ti. However, apatites from carbonatites have deeper anomalies of Zr-Hf and Nb. They also have lower Th, U, and Pb contents compared to the rocks of alkaline series. Apatites in the rocks of alkaline series have high Th and Pb contents (Figure 6a). The spidergram of apatite from carbonate–silicate rocks is close to that of alkaline rocks.

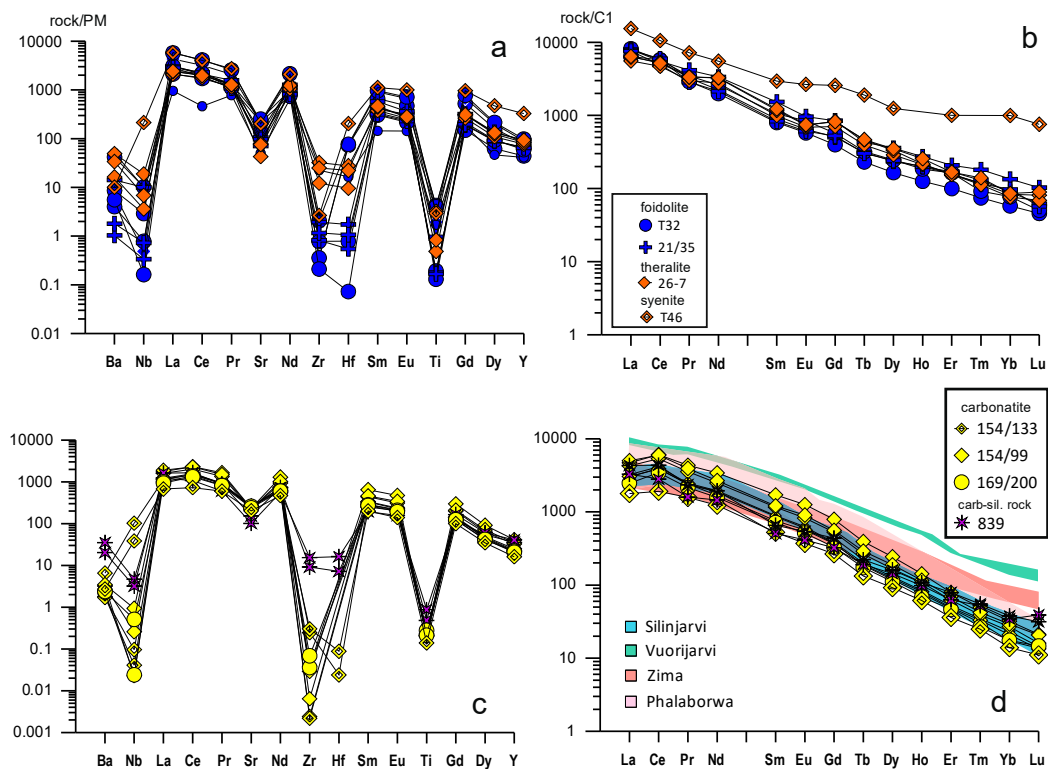


Figure 6. REE and trace-element distribution in the apatites from alkaline silicate (a,b) and carbonate–silicate rocks and carbonatites (c,d) of the Tikshezero complex. Concentrations are normalized to chondrite and primitive mantle after [10]. Fields shown in (d) were plotted using data from [12–15].

The analyzed apatites show similar chondrite-normalized LREE-enriched patterns (Table 4, Figure 6b). Apatites from carbonatites have a higher REE fractionation ((La/Yb)_n = 128–176), whereas apatites in rocks of the alkaline series are less fractionated ((La/Yb)_n = 54–110), and apatites in the carbonate–silicate rocks have an intermediate REE fractionation ((La/Yb)_n = 96–114) (Figure 4b,d). All apatites show no negative Eu anomaly. The total REE content in apatites varies from 6742 to 23,181 ppm, showing no systematic variations depending on the rock type (Table 4).

4.3.3. Zoning

Apatite in theralite shows an outward increase in F from 3.83–3.94 to 4.04–4.64, P₂O₅, Mn, Na, and Y are practically absent. The mineral is characterized by the high contents

of La, Ce, and Nd with insignificant contents of Pr. The total REE contents decrease to rims, which is reflected in the lighter luminescence. The Sr content weakly varies within 0.25–0.32. The SiO₂ content decreases to rims from 1.99–0.59 to 0.37–0.28 wt % (Table S1).

Apatite in ijolite–melteigite is turbid and shows no zoning. The total REE content is lower, with the predominance of Ce. It contains (in wt %) 0.36–0.40 Sr, 0.16–0.32 FeO, and 0.36–0.66 SiO₂. Y, SO₃, Mn, and Na₂O are practically absent (Table S1).

In syenite, grains have compositional, frequently nonsystematic heterogeneity. Some grains with light luminescence have a lower P₂O₅ content, but higher La₂O₃, Ce₂O₃ (within 2.36–0.62 in this sample), Pr₂O₃, SiO₂ (reaching highest contents of 3.06–0.71 among the studied apatites), Nd₂O₃, and Y₂O₃ above detection limits (also decreases in dark areas), which is practically absent in other apatites. SrO shows practically no variations, and its content is lower than in theralites and ijolite–melteigites (Table S1).

In apatites from silicate–carbonate rocks, the F content decreases from 3.20–2.90 to 3.14–2.54 wt %. The mineral shows weakly expressed oscillatory zoning for P₂O₅, Ce₂O₃, Nd₂O₃, and Na₂O, with a decrease in their contents in the intermediate parts. Compared to the above-described apatites, this apatite shows a significant increase in SrO, absence of Y₂O₃, and a practically complete absence of SiO₂, with the appearance of a significant amount of Na₂O (0.16–0.36) (Table S1).

In vaguely patched apatite from carbonatites, variations in elements are practically absent or insignificant and nonsystematic. Among REE, it has notable contents of Ce₂O₃ (0.16–0.50) and Nd₂O₃ (0.11–0.25). SiO₂ is absent. Na₂O varies from 0.17 to 0.31, and SrO varies from 0.44 to 0.56. The total REE content is slightly more than 1%. (Table S1).

4.4. Carbonates

The analysis of major components showed that carbonates in the studied rocks are mainly represented by calcite. In alkaline rocks, it is present in accessory amounts as small interstitial grains and fine veinlets. In carbonate–silicate rocks, calcite (2–3 mm) composes ~50 vol% of the rock. In carbonatites, carbonates together with apatite are cumulus minerals. Calcite forms grains of irregular shape, which compose up to 80%. Carbonatites also contain dolomite as rims around the accumulations of phlogopite, alkaline amphibole, and apatite [5].

In calcites from foidolites, SrO and BaO are absent, while the MgO, MnO, and SrO contents are lower than in carbonates from carbonatites. A distinctive feature of calcite in the carbonate–silicate rocks is the presence of BaO. In the spidergrams, dolomites and calcites from carbonatites have deep Zr and Ti minimums. Calcites from foidolites and carbonate–silicate rocks reveal only insignificant negative Ti and Nb anomalies (Figure 7a).

Calcite from carbonatites has a moderate REE fractionation ((La/Yb)_n = 4.78–17.82), and moderately low fractionation of LREE ((La/Sm)_n = 1.22–2.83) and HREE ((Gd/Yb)_n = 2.36–3.82) (Table 5). Dolomite sharply differs from calcite in a strongly fractionated REE pattern ((La/Yb)_n = 139–158, (La/Sm)_n = 5.99–6.40, (Gd/Yb)_n = 7.69–11.95). Calcites have a higher total REE (128–360 ppm) than the dolomites' REE of 94–99. Calcites from carbonate–silicate rocks show similar REE patterns, but a slightly lower total REE (Figure 7b).

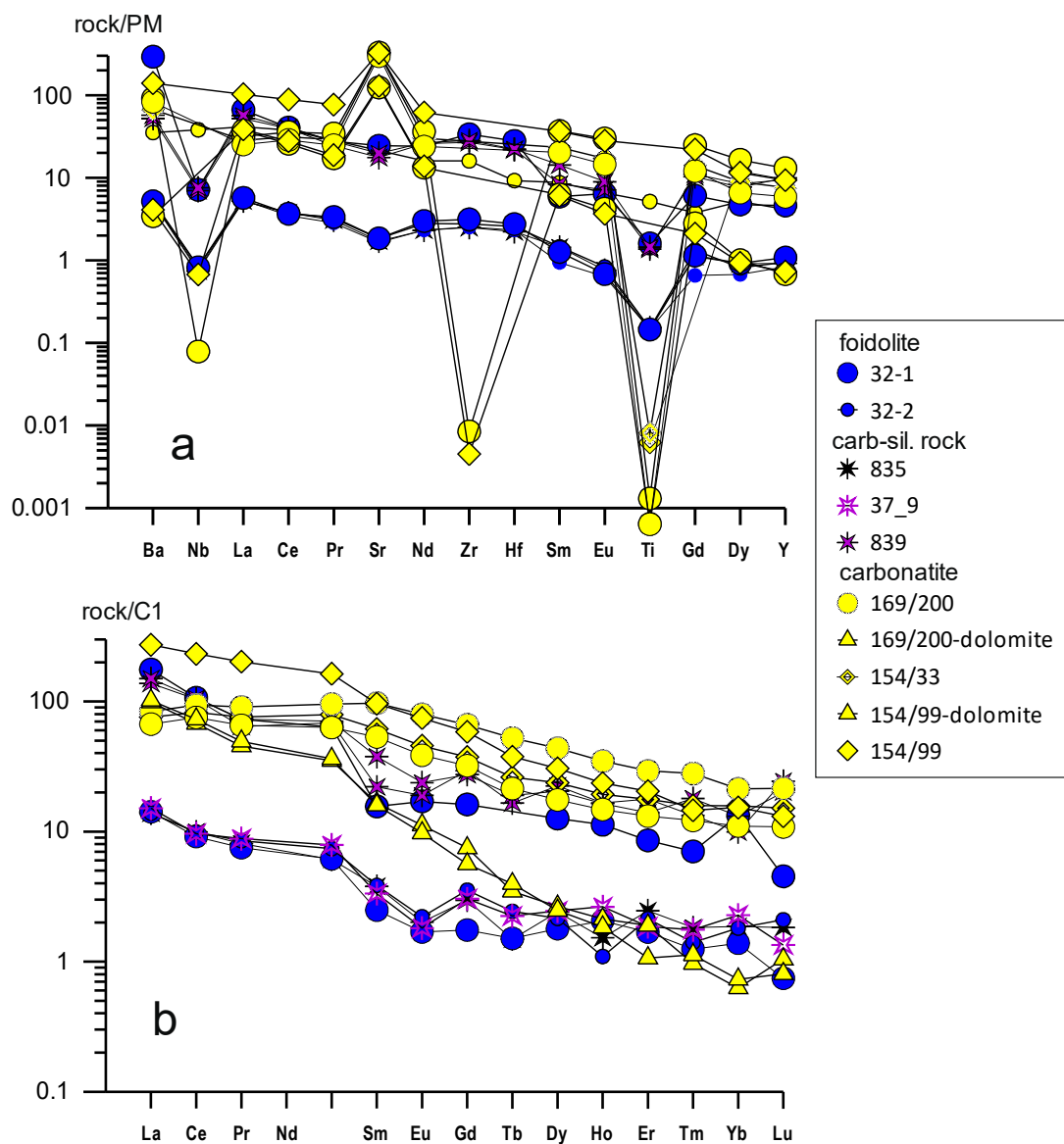


Figure 7. Trace-element (a) and REE (b) distribution patterns in the carbonates from rocks of the Tikshezero complex. Concentrations are normalized to chondrite and primitive mantle after [10].

Table 5. Trace-element composition of carbonates from the Tikshezero complex.

Sample	32-1	32-2	154/99		169/200				154/133		839	37-9	835	
Rock	Melteigite-Ijolite			Carbonatite									Carb-Sil	
Rb	170	3.08	2.56	0.01	0.00	0.02	bdl	bdl	bdl	bdl	33.7	30.40	2.80	3.09
Sr	486	36.43	32.9	6503	2577	5908	2471	6515	6487	7486	394	350	36.7	34.0
Y	19.8	4.09	3.60	40.15	3.15	25.3	2.93	56.2	32.8	40.9	42.9	40.7	4.65	3.95
Zr	353	28.89	26.6	bdl	0.05	bdl	bdl	0.09	bdl	bdl	297	281	32.9	26.3
Nb	4.70	0.55	0.50	bdl	0.44	bdl	bdl	0.05	bdl	bdl	4.97	4.60	0.54	0.49
Ba	1930	34.80	33.7	922	27.0	549	22.6	603	445	587	378	345	34.3	33.2
La	43.0	3.39	3.47	66.7	24.9	16.4	24.2	20.5	18.5	106	36.7	33.7	3.70	3.39

Table 5. Cont.

Sample	32-1	32-2	154/99		169/200			154/133		839		37-9		835
Rock	Melteigite–Ijolite			Carbonatite					Carb–Sil					
Ce	68.0	6.33	5.84	148	46.6	48.1	43.2	59.9	52.5	213	67.5	66.4	6.14	6.33
Pr	7.03	0.82	0.72	19.5	4.76	6.3	4.37	8.74	7.33	23.6	7.05	6.19	0.85	0.78
Nd	30.1	3.50	2.92	77.3	17.2	29.9	16.6	45.3	37.6	98.7	33.4	32.50	3.74	2.90
Sm	2.40	0.59	0.38	14.8	2.46	8.22	2.54	15.0	9.47	17.3	5.80	3.40	0.51	0.58
Eu	0.99	0.13	0.10	4.32	0.56	2.24	0.65	4.61	2.65	4.35	1.38	1.10	0.11	0.12
Gd	3.30	0.72	0.36	11.9	1.15	6.56	1.53	13.5	7.65	11.6	5.60	6.00	0.62	0.60
Tb	bdl	0.09	0.06	1.41	0.15	0.80	0.13	1.96	0.98	1.47	0.71	0.62	0.08	0.06
Dy	3.20	0.55	0.46	7.77	0.63	4.45	0.68	11.1	6.03	8.05	5.20	5.70	0.62	0.61
Ho	0.64	0.06	0.12	1.34	0.10	0.84	0.12	1.97	1.10	1.43	0.93	0.94	0.15	0.09
Er	1.42	0.35	0.28	3.40	0.18	2.18	0.31	4.86	2.94	3.90	2.32	2.95	0.31	0.41
Tm	0.18	0.04	0.03	0.37	0.03	0.31	0.02	0.72	0.41	0.52	0.46	0.34	0.05	0.05
Yb	2.20	0.30	0.23	2.53	0.12	1.82	0.10	3.52	2.61	2.78	2.17	1.64	0.38	0.31
Lu	0.12	0.05	0.02	0.33	0.02	0.28	0.03	0.55	0.38	0.46	0.51	0.62	0.03	0.05
Hf	7.90	0.73	0.66	bdl	bdl	bdl	bdl	bdl	bdl	bdl	6.30	6.20	0.78	0.63
Ta	0.60	0.04	0.04	bdl	0.03	bdl	bdl	bdl	bdl	bdl	0.39	0.51	0.05	0.06
Pb	36.6	6.26	5.77	3.02	1.22	1.16	1.41	1.50	0.74	2.99	67.0	67.8	5.79	6.52
Th	8.19	0.79	0.77	bdl	bdl	bdl	0.01	0.00	bdl	bdl	8.29	7.83	0.93	0.78
U	2.44	0.59	0.49	bdl	0.06	bdl	0.00	0.00	bdl	bdl	4.88	5.41	0.45	0.48

5. Discussion

5.1. Relations of Ultramafic–Mafic and Alkaline Series Based on Comparison of Clinopyroxenes

An important petrological problem of the Tiksheozero complex is the origination of low-alkali mafic–ultramafic cumulates and their relations with alkaline rocks of the second phase. In our previous studies, we suggested that the initial melts of both series were derived from a similar mantle source but at different depths under different conditions [5,6], although some arguments were reported in favor of the formation of cumulates through the crystallization of alkaline ultramafic melts [5]. In attempts to solve this problem, we carried out a detailed comparable analysis of pyroxene composition.

Relative to ultramafic rocks, clinopyroxenes in all alkaline rocks are enriched in incompatible elements and sharply depleted in Cr (Figure 3 and Figure 8b–d).

A distinctive feature of clinopyroxenes from ultramafic–mafic rocks is the high Mg number (Mg# varies from 77 in the gabbroids to 93 in pyroxenites) (Figure 8a). With decreasing Mg#, clinopyroxene shows an increase in Al₂O₃, Na₂O, and TiO₂ with a decrease in CaO (Figure 8a,b).

In all the variation diagrams, there is a gap between clinopyroxenes from ultramafic low-alkali and alkaline rocks, which is most significant in the Al₂O₃, TiO₂, and Cr–Mg# diagrams (Figure 8a,b) and for some incompatible elements (Nd, Hf, Zr, and others) (Figure 8c,d), which are low in the ultramafic rocks. In the Na₂O–Mg# diagram (Figure 8a), the rocks define a single trend. It should be noted that in some diagrams, the data points of clinopyroxene from gabbroic rocks partly fill this gap, approaching compositions of clinopyroxenes from alkaline rocks.

Clinopyroxenes from rocks of the low-alkali and alkaline series define very close trends in the *Hd–Di–Aeg* diagram (Figure 9), evolving to a higher Fe composition. It is seen that the trend of the low-alkali series is slightly displaced relative to other rocks to the lower part of the diagram. The evolution trends of the pyroxenes of the Tiksheozero complex

(Figure 9) are close to those of the Jacupiranga and Banhadao complexes in Brazil [16,17]. The trace-element composition of clinopyroxenes is presented in Table 2.

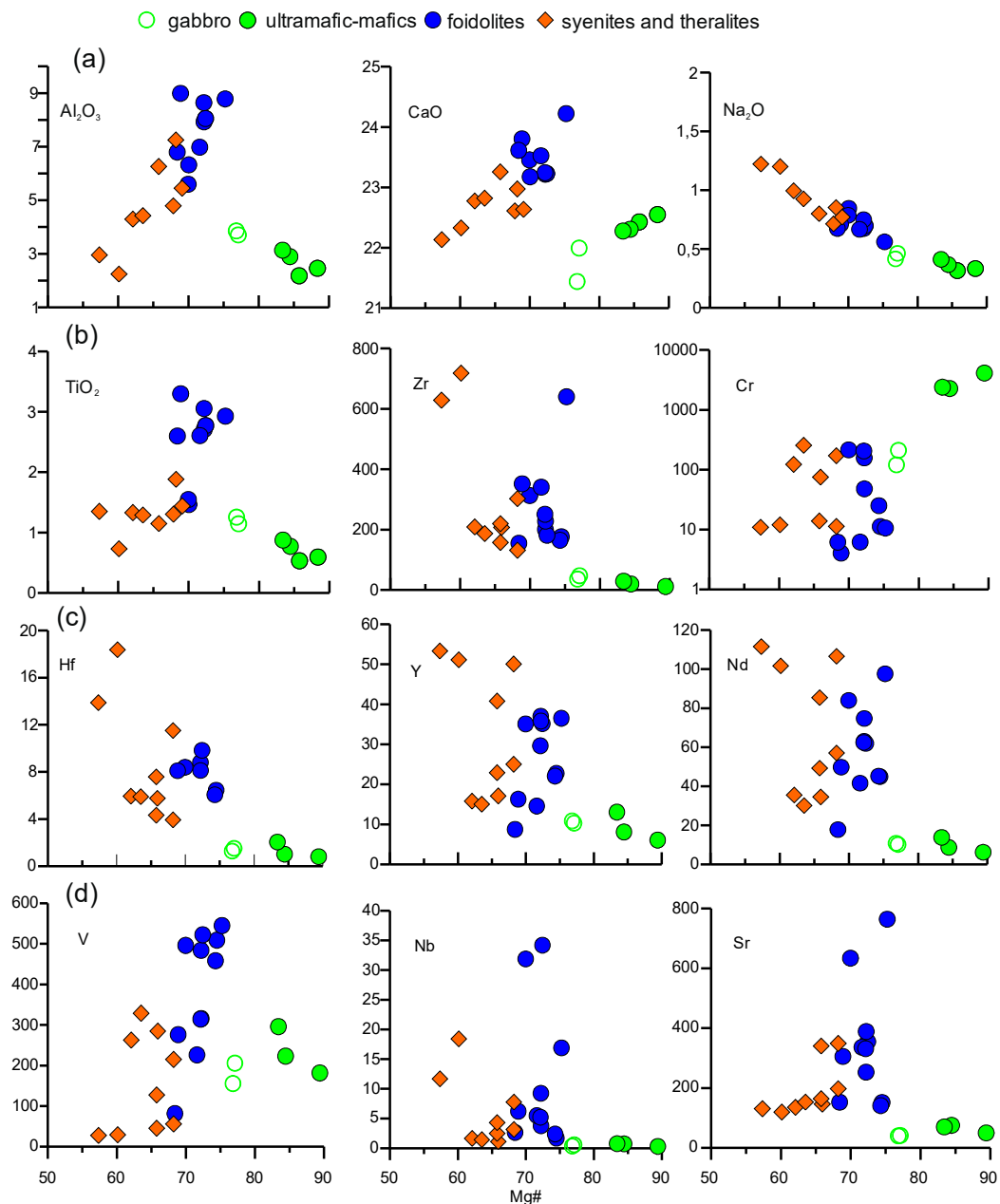


Figure 8. Major and trace elements versus Mg# for clinopyroxenes from the Tikshezero complex. Major element compositions of clinopyroxenes are listed in [5].

It is known that the Al_2O_3 content in clinopyroxene is controlled by the composition of initial magma, in particular, the SiO_2 content [18,19]. Clinopyroxenes that crystallized from tholeiitic magmas have a high Si/Al ratio [20]. Clinopyroxenes from the low-alkali ultramafic–mafic rocks have 2.18%–3.59% Al_2O_3 and a relatively high SiO_2 content (>50 wt %). Clinopyroxene from the second phase, especially from foidolites, has higher Al_2O_3 and low SiO_2 contents (<50), which unambiguously indicate the formation from silica-undersaturated magma. At the same time, it was noted [21] that clinopyroxenes, the derivatives of the silica-undersaturated magmas, are characterized by a high CaO content, while those of the low-alkali ultramafic rocks have a high CaO content close to that of the

second phase. The relations between Ti and Ca + Na in clinopyroxene were also used to determine the alkalinity of the initial melts [22].

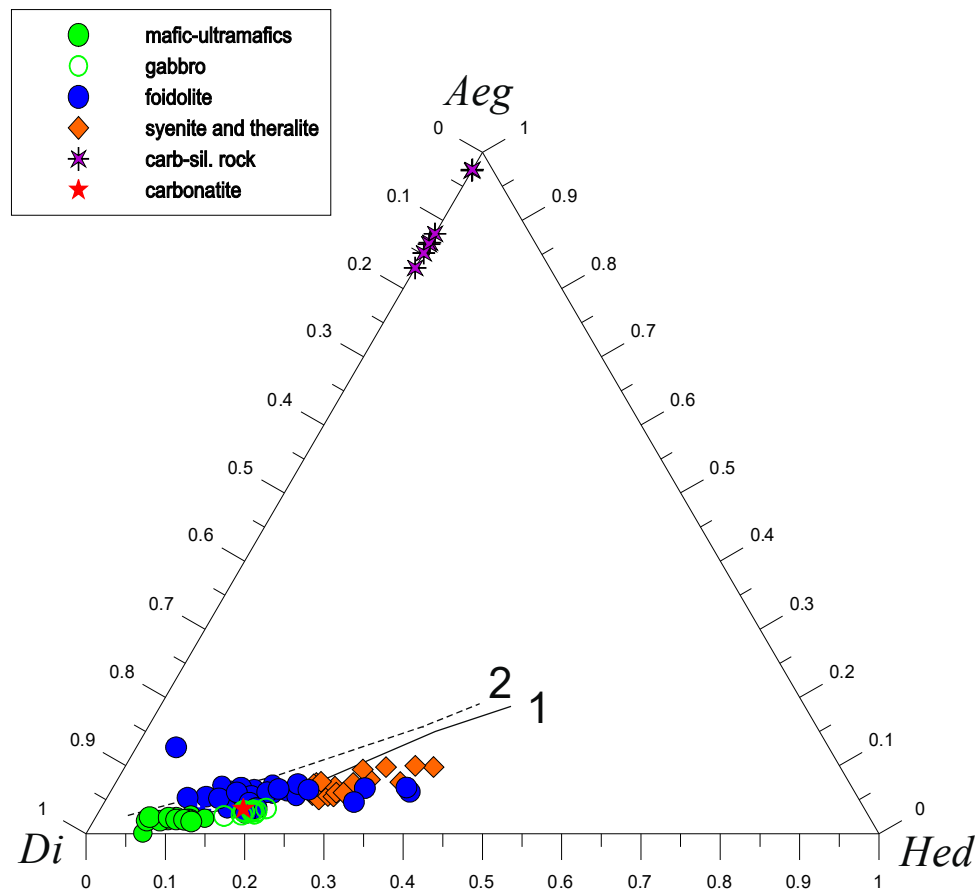


Figure 9. Compositions of clinopyroxenes from the rocks of the Tikshezero massif in the Di–Hed–Aeg diagram. Variation trends of clinopyroxenes shown for comparison: (1) Jacupiranga, Brazil; (2) Banhadao, Brazil [16,17]. Major element compositions of clinopyroxenes are listed in [5].

It is seen in the $\text{SiO}_2\text{-Al}_2\text{O}_3$ diagram (Figure 10a) that in spite of the fact that compositions of clinopyroxenes from the ultramafic–mafic series plot in the field of non-alkaline rocks, all studied pyroxenes define a common trend with clinopyroxenes from alkaline rocks, approaching the boundary with a normal-alkaline series. In the Ti–Ca+Na diagram (Figure 10b), clinopyroxenes from the ultramafic–mafic series plot in the field of alkaline rocks. The gap between the series is partly filled with clinopyroxenes from gabbros collected in the upper part of the section, the transitional character of which is seen in the Na_2O , Al_2O_3 , Cr, and TiO_2 diagrams versus Mg# (Figure 8). It was previously assumed that ultramafic–mafic and alkaline series were formed at different depths [6]. In this work, we attempted to qualitatively estimate the relative depth of rock formation using pyroxene compositions. In pyroxenes, Al coordination is determined by pressure and has an important petrogenetic significance. The high pressure facilitates the preferable accumulation of Al in the octahedral site, and, respectively, a decrease in the $\text{Al}^{\text{IV}}/\text{Al}^{\text{VI}}$ ratio (Figure 11a). These facts were used to develop the $\text{Al}^{\text{IV}}\text{-Al}^{\text{VI}}$ diagram [20], where clinopyroxenes from the studied rocks fall in the field of moderate pressure, practically on a single trend, i.e., have close $\text{Al}^{\text{IV}}/\text{Al}^{\text{VI}}$ ratios and, respectively, were formed at close pressures. The Ti/Al ratio in clinopyroxenes is also determined by pressure: an increase in pressure is favorable for Al involvement in clinopyroxene, and, respectively, causes a decrease in the Ti content in its lattice. Hence, with increasing pressure, this ratio tends to decrease. According to the diagram (Figure 11b), we also suggest that these rocks were formed at moderate pressures.

Thereby, this ratio for rocks of the given series is close, which also suggests their formation at close pressure.

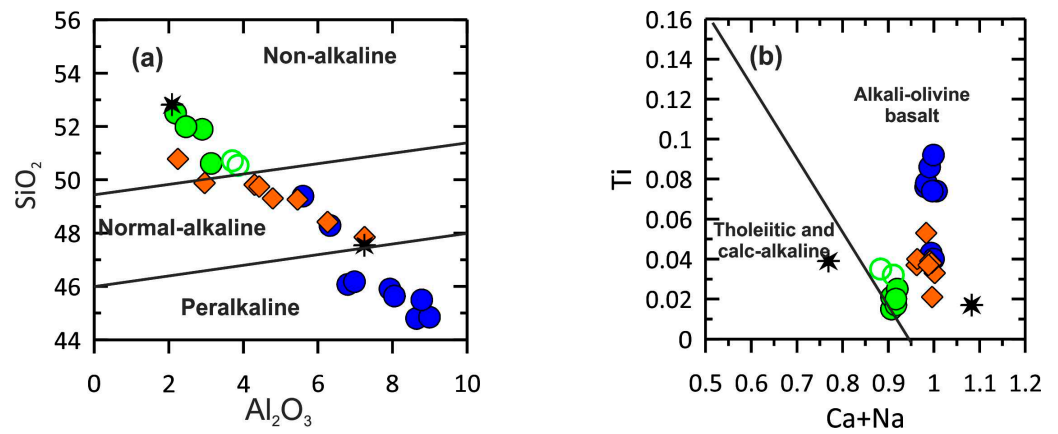


Figure 10. Variations in Ti vs. Ca+Na (a) and SiO₂ vs. Al₂O₃ (b) for clinopyroxenes from rocks of the Tikshezzero complex. Fields after [18,19]. For symbols, see Figure 9.

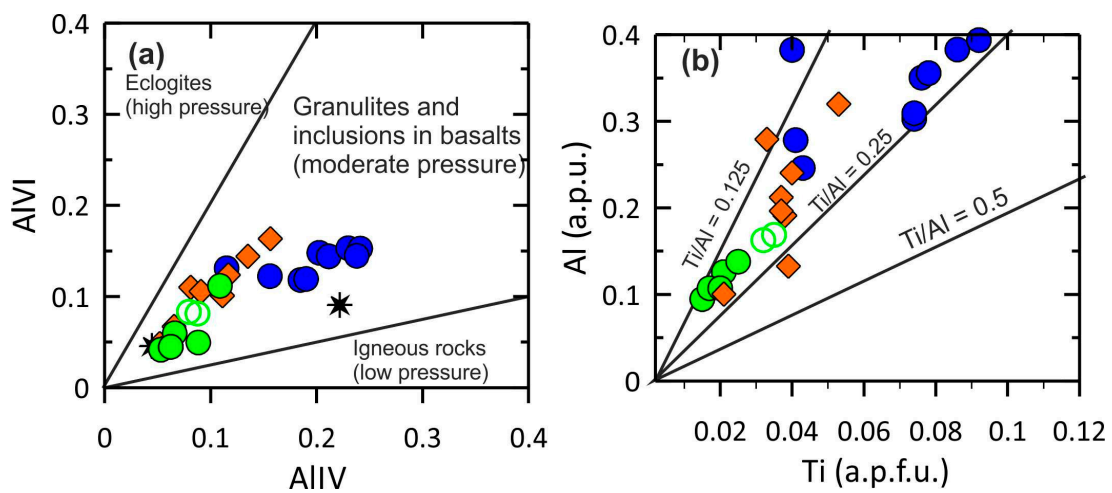


Figure 11. AlVI vs. AlIV (a) and Al-Ti (b) diagrams for clinopyroxenes from the rocks of the Tikshezzero complex. Fields after [20]. For symbols, see Figure 9.

At the same time, clinopyroxenes from different rocks sharply differ in REE fractionation (Figure 12). Clinopyroxenes from low-alkali mafic-ultramafic rocks define a distinct trend, which marks a much lower LREE and REE fractionation compared to those of other series (Figure 12). Some scatter in the data points of alkaline rocks is likely related to the late metasomatic alterations. In particular, the lower REE fractionation in clinopyroxenes from syenites is consistent with some HREE enrichment observed in apatites from these rocks (see below), which likely reflect the late magmatic alterations through the interaction with fluid.

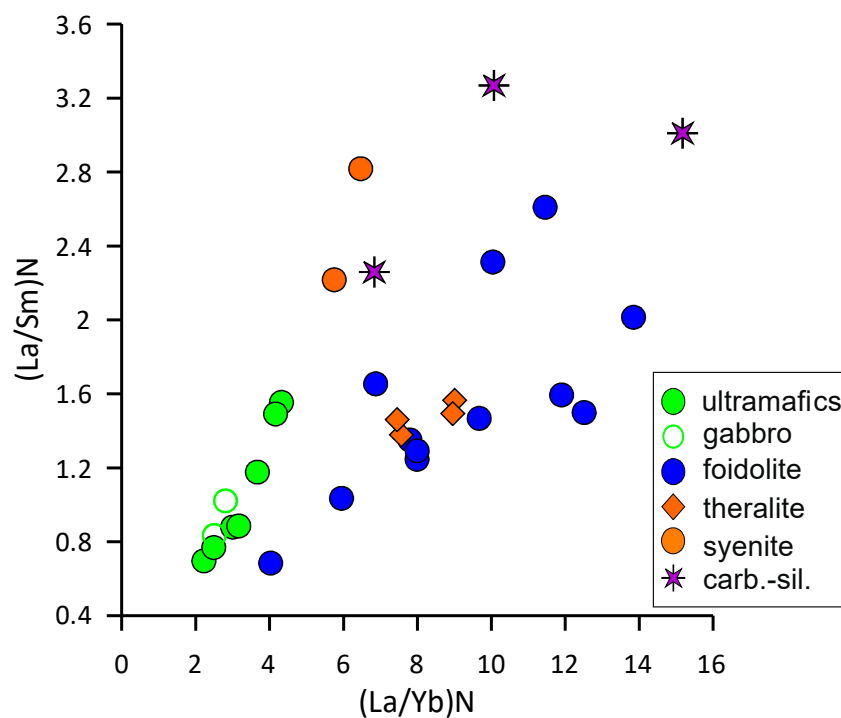


Figure 12. (La/Sm)_N-(La/Yb)_N diagram for clinopyroxenes from rocks of different series of the Tikshezero complex.

At the same time, in spite of the differences, practically all studied pyroxenes, except for pyroxenes from carbonate–silicate rocks, are characterized by the slightly convex-upward spectra ($La/Nd < 1$), which are typical of deep-seated cumulates formed in equilibrium with an alkaline basaltic melt (Figure 3b,d,f) [23]. Obtained data are well consistent with our previous modeling [5]. In the cited paper, we calculated the REE composition of the melt in equilibrium with clinopyroxene from the low-alkali ultramafic rock of the complex, wehrlite. It was demonstrated that the REE distribution pattern of the modeled liquid is practically identical to those of melteigite dike and theralite (Figure 12 in [5]), which indicates that the low-alkali ultramafic cumulates could be formed through the crystallization of an alkaline ultrabasic (nephelinite) melt. The fact that the low-alkali ultramafic rocks could be cumulates of alkaline series also follows from close clinopyroxene trends in the *Di-Aeg-Hd* diagram (Figure 9).

Variations in Hf–Sm relations can be used to estimate the contribution of different agents to their genesis. A positive correlation of these elements with their simultaneous increase observed in the studied clinopyroxenes suggests their origination through fractional crystallization from a silicate melt, whereas the contribution of aqueous fluid would cause an increase in the Sm content at a practically constant Hf content [24]. In the studied clinopyroxenes, these elements correlate with a correlation coefficient of 0.86, which excludes the contribution of aqueous fluid.

5.2. Magmatic and Post-Magmatic Evolution of Massif Deduced from Apatite Study

Our study showed that apatites from diverse rocks of the Tikshezero complex are characterized by the different morphology and luminescence, and, correspondingly, different trace-element composition. Euhedral magmatic apatite in theralite shows a typical undisturbed normal magmatic zoning, which likely reflects a decrease in the REE content in the melt at the final stages of the magmatic crystallization of the rocks.

The precipitation of monazite along the fractures and rims of apatite in a complex with a turbid texture, LREE decrease, and enrichment in HREE and Y in apatite from syenites are indicative of the metasomatic interaction with fluid and, respectively, processes of dissolution–precipitation [25,26]. The grains where monazite is not formed have a higher

LREE content and lesser contrast between the core and rim. However, in spite of the metasomatic reworking and some disturbance, the apatite retained primary magmatic zoning, with an REE decrease to the grain rims.

Microprobe analyses showed that apatites from carbonatites have a weakly expressed heterogeneity with an insignificant outward increase in REE. Similar REE zoning is observed in apatites from carbonate–silicate rocks.

Thus, the studied apatite shows two types of REE zoning. The first type is characterized by the outward REE decrease, which is reflected in the lighter cathodoluminescence in rims. This type of zoning is typical of apatites from the alkaline silicate rocks of the complex. It is suggested that the apatite content was sufficiently high to deplete a residual melt in REE. Such a trend likely indicates that apatite was overgrown from residual melt pockets in interstices at the late-magmatic stage. Hence, the system was closed, while new melt batches, and, respectively, new REE contribution, were absent. Thus, zoning of the latter reflects the initial magmatic zoning of apatite in alkaline rock. In some rocks (syenites), this tendency was slightly disturbed by the late interaction with fluid. In contrast, apatite from carbonatite and carbonate–silicate rock shows an insignificant REE increase to the margin, without a clearly expressed visual zoning. This is likely related to the diffusion re-equilibration of newly formed apatite with a fresh portion of LREE-enriched carbonatite magma. The absence of isotope evidence for crustal contamination [6] confirms this hypothesis. The presence of Na in apatite from carbonatites and carbonate–silicate rocks suggests that the emplacement of carbonatites was accompanied by an influx of Na fluid.

Similar types of zoning are observed in many alkaline complexes with carbonatites [13,14].

5.3. Relations of Silicate Rocks and Carbonatites

The steady spatial association of ultramafic rocks, alkaline silicate rocks, and carbonatites in many complexes worldwide raises a question concerning their genetic relation. Our previous studies showed [6] the extremely narrow variations in their isotopic parameters. At the same time, the nature of their petrogenetic relation remains unclear. According to the generally accepted genetic models, carbonatites represent a residual product of advanced fractional crystallization of a common magma [26,27] or were formed through liquid immiscibility between carbonatite and alkaline silicate melts (e.g., [28,29]). The second model is supported by the accumulation of LREE and Na₂O, and depletion in HREE and HFSE, which is consistent with partition coefficients between silicate and carbonatite melts [30]. However, direct evidence in support of the immiscibility such as spherulites or carbonate globule are absent, while minerals in carbonatites and associated rocks differ in composition. When liquid immiscibility occurs, compositions of minerals crystallizing from the two liquids should be close. In addition, LREE and other incompatible elements are accumulated in the final derivatives during fractional crystallization, i.e., in carbonatites. Apatites in carbonatites of the Tikshezero complex are enriched in LREE, U, and Y relative to the alkaline silicate rocks, whereas the Zr and Nb contents are lower. In the Y–Ho diagram (Figure 13), all rocks of the complex define a distinctive linear trend, with a near-chondritic average Y/Ho ratio of 24.8. Thereby, the Y/Ho ratio decreases from 31–24 in silicate rocks to 20 in carbonatites. Such a decrease could be related to the fractionation of the Y-rich phase in carbonatites. According to [13], such a phase could be both a high-Y mineral (e.g., monazite or xenotime) and fluid entrapped in the carbonatite.

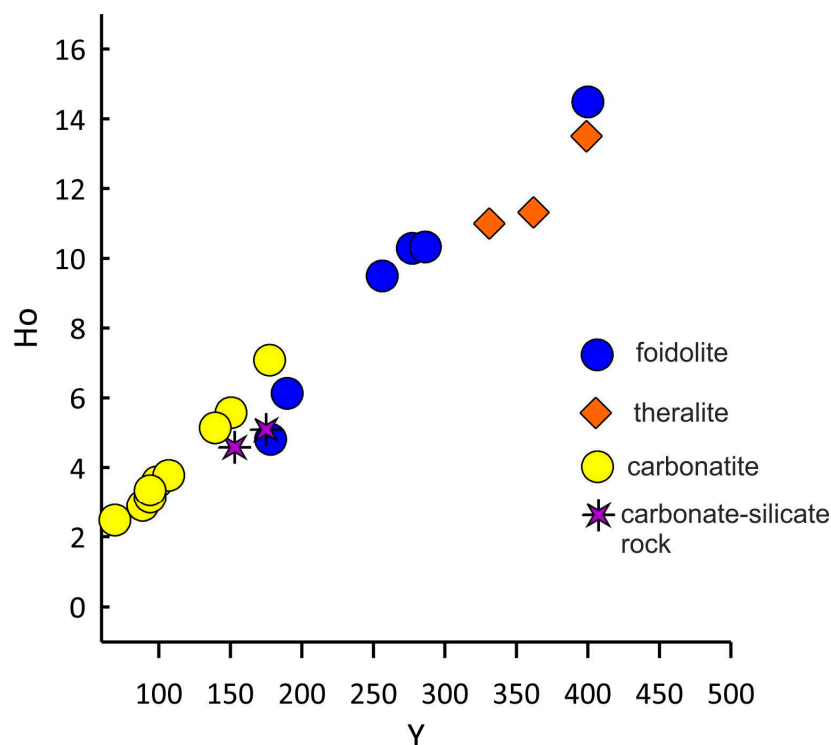


Figure 13. Y–Ho diagram for apatite from the rocks of the Tikshezero complex.

The fact that the apatites from alkaline rocks and carbonatites of the complex plot on the common trend indicates that they are genetically related. An increase in Na and REE and a decrease in the Y/Ho ratio from theralites and foidolites to carbonatites likely suggests that the evolution of the complex was controlled via fractional crystallization.

Some authors [31] report experimental and geochemical data, which suggest that alkaline melts bear evidence for the open-system carbonate fluxing (carbonate metasomatism) at different mantle depths during magma generation. These data also argue against a primary carbonate–silicate immiscibility.

5.4. Comparison with Carbonatite Complexes Worldwide

Apatites from the studied complex were compared to those from analogous complexes worldwide of a different age in an attempt to reveal whether ancient carbonatite complexes have a peculiar composition. As mentioned above, the Tikshezero is the world's oldest complex containing the entire spectrum of rocks from ultramafic cumulates through foidolites and syenites, and theralites to carbonatites. Carbonatite complexes of close ages usually have a more narrow rock spectrum. In particular, the oldest Neoproterozoic Siilinjärvi complex (2613 ± 18 Ma, [32]) also located at the Karelian craton consists exclusively of rocks of the glimmerite–carbonatite series [33], whereas rocks of the foidolite and syenite series are absent. The Phalaborwa massif of a similar age ~ 2.06 Ma [34], in addition to carbonatites, also contains pyroxenites and phoscorites, as well as nearby syenite dikes [14,34], but are devoid of foidolites. The Belaya Zima carbonatite complex with an age of 645 ± 6 Ma [15] and Vuorijärvi intrusion with an age between 375 ± 7 and 383 ± 7 Ma [35] were taken as the younger analogues. The Belaya Zima complex consists of carbonatites, foidolites, and nepheline syenites [15]. The Vuorijärvi intrusion is located on the Kola Craton and includes the wide rock spectrum: ultramafic cumulates (wehrlites, dunites, clinopyroxenites), foidolites, and carbonatites. It can be seen in Figure 6d that the REE patterns of apatites from carbonatites of the Tikshezero complex are almost completely overlapped with those of the oldest Siilinjärvi complex. Apatites from carbonatites of the Phalaborwa massif have a higher REE level with a similar shape in the REE pattern. At the same time, the younger carbonates from the Zima and Vuorijärvi complexes differ in the lower degree

of REE fractionation with higher HREE contents. The difference between older and younger (<1 Ga) carbonatites was mentioned by [36] based on the study of Nd, Hf, and S isotopic composition. These authors related this difference in an increase in the recycled crustal component owing to the transition to the modern plate tectonics at a lower geothermal gradient during Late Proterozoic [37]. As also seen in the diagrams proposed in [38], especially in $(Ce/Yb)_N$ –REE, %, apatites from carbonatites of the Tikshezero complex resemble apatites from ancient Phalaborwa and Sillinjärvi massifs, whereas apatites from silicate rocks show no such tendency (Figure 14).

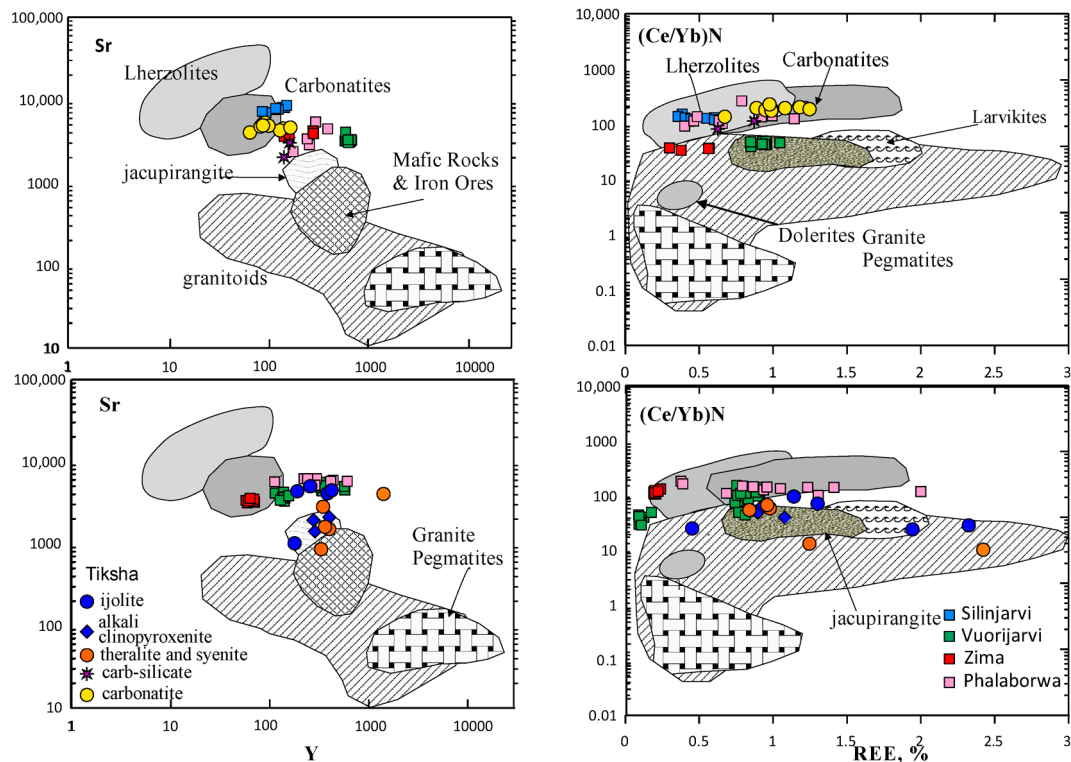


Figure 14. Compositions of rocks from the Tikshezero complex compared to those of the Sillinjärvi, Vuorijärvi, Belaya Zima, and Phalaborwa [13–16] complexes in the diagram [38].

6. Conclusions

- (1) Examination of clinopyroxene in the rocks of the Tikshezero complex allowed us to suggest that the low-alkali ultramafic–mafic rocks of the complex are comagmatic to alkaline rocks and were formed from an alkaline basaltic melt under close moderate pressures.
- (2) Cathodoluminescence imaging revealed different apatite textures in different rock types, which correspond to a distinct trace-element composition. Apatite from melteigit shows no zoning. Apatite from theralite reveals a clearly observed normal magmatic zoning with an outward LREE decrease, which is related to the closed-system fractional crystallization from residual melt pockets. Apatite in syenite retained weak normal magmatic zoning, which was slightly disturbed by the interaction of this rock with fluid. Apatite from carbonatite is characterized by an insignificant LREE increase to margins, which is likely related to the re-equilibration of previously formed apatite with fresh batches of REE-enriched carbonatite magma.
- (3) The absence of signs of liquid immiscibility in combination with a common trend of apatites from alkaline rocks and carbonatites in the Y–Ho diagram, a decrease in the Y/Ho ratio in apatites from foidolites to carbonatites, and different trace-element compositions of apatite in silicate rocks and carbonatites, as well as the accumulation of incompatible elements in apatites from carbonatites, serve as arguments in support of their origin through fractional crystallization rather than through liquid immiscibility.

Supplementary Materials: The following supporting information can be downloaded at: <https://www.mdpi.com/article/10.3390/min13101318/s1>. Table S1: representative composition of apatite from the Tiksheozero complex. Figure S1: microphoto and CL images of apatite from sample T32. Figure S2: BSE and CL images of apatite from syenite T46. Figure S3: BSE and CL images of apatite from sample 835. Figure S4: BSE, CL images and microphotos of apatite from carbonatites, samples 154/99 (A), 154/133 (B), and 169/200 (C and D).

Author Contributions: Conceptualization, M.B., data curation, M.B. and A.C.; investigation, M.B., A.C., E.S., E.K. and T.G.; methodology, M.B., E.K. and T.G., writing—original draft, M.B., A.C. and E.S.; writing—review and editing, M.B. and A.C. All authors have read and agreed to the published version of the manuscript.

Funding: This study was carried out in the framework of the State Assignment of the Institute of Geology of Ore Deposits, Petrography, Mineralogy and Geochemistry, Russian Academy of Sciences (no. 121041500222-4).

Data Availability Statement: No applicable.

Conflicts of Interest: The authors declare no conflict of interest.

References

1. Sharkov, E.; Bogina, M.; Chistyakov, A. Magmatic systems of large continental igneous provinces. *Geosci. Front.* **2017**, *8*, 621–640. [[CrossRef](#)]
2. Corfu, F.; Bayanova, T.; Shchiptsov, V.; Frantz, N. U-Pb ID-TIMS age of the Tikshozero carbonatite: Expression of the 2.0 Ga alkaline magmatism in Karelia, Russia. *Cent. Eur. J. Geosci.* **2011**, *3*, 302–308.
3. Tichomirowa, M.; Whitehouse, M.; Gerdes, A.; Götze, J.; Schulz, B.; Belyatsky, B. Different zircon recrystallization types in carbonatites caused by magma mixing: Evidence from U-Pb dating, trace element and isotope composition (Hf and O) of zircons from two Precambrian carbonatites from Fennoscandia. *Chem. Geol.* **2013**, *353*, 173–198. [[CrossRef](#)]
4. Rodionov, N.V.; Belyatsky, B.A.; Antonov, A.V.; Presnyakov, S.L.; Sergeev, S.A. Baddeleyite U-Pb SHRIMP II age determination as a tool for carbonatite massifs dating. *Dokl. Earth Sci.* **2009**, *428*, 1166–1170. [[CrossRef](#)]
5. Sharkov, E.V.; Chistyakov, A.V.; Bogina, M.M.; Shchiptsov, V.V.; Belyatsky, B.V.; Frolov, P.V. Petrology of the Mid-Paleoproterozoic Tiksheozero ultramafic-alkaline-carbonatite complex (Northern Karelia). *Petrology* **2021**, *29*, 478–507. [[CrossRef](#)]
6. Bogina, M.; Belyatsky, B.; Sharkov, E.; Chistyakov, A.; Krymsky, R. Origin of the Middle Paleoproterozoic Tiksheozero ultramafic-alkaline-carbonatite complex, NE Fennoscandian Shield: Evidence from geochemical and isotope Sr-Nd-Hf-Pb-Os data. *Minerals* **2021**, *11*, 570. [[CrossRef](#)]
7. Ivashchenko, V.I.; Golubev, A.I. *Gold and Platinum of Karelia: Genetic Types of Mineralization and Prospects*; Karelian Science Centre: Petrozavodsk, Russia, 2011. (In Russian)
8. Reguir, E.P.; Chakhmouradian, A.R.; Pisiak, L.; Halden, N.M. Trace-element composition and zoning in clinopyroxene- and amphibole-group minerals: Implications for element partitioning and evolution of carbonatites. *Lithos* **2012**, *128–131*, 27–45. [[CrossRef](#)]
9. Morimoto, N. Nomenclature of pyroxenes. *Mineral. Mag.* **1988**, *52*, 535–550. [[CrossRef](#)]
10. McDonough, W.F.; Sun, S.-S. The composition of the Earth. *Chem. Geol.* **1995**, *120*, 223–253. [[CrossRef](#)]
11. Leake, B.E.; Woolley, A.R.; Arps, C.E.; Birch, W.D.; Gilbert, M.C.; Grice, J.D. Nomenclature of amphiboles: Report of the subcommittee on amphiboles of the International Mineralogical Association on new minerals and mineral names. *Can. Mineral.* **1997**, *35*, 219–246.
12. Decrée, S.; Savolainen, M.; Mercadier, J.; Debaille, V.; Hohn, S.; Frimmel, H.; Baele, J.-M. Geochemical and spectroscopic investigation of apatite in the Siilinjärvi carbonatite complex: Keys to understanding apatite forming processes and accessing potential for rare-earth elements. *Appl. Geochem.* **2020**, *123*, 104778. [[CrossRef](#)]
13. Brassinness, S.; Balaganskaya, E.; Demaiffe, D. Magmatic evolution of the differentiated ultramafic, alkaline and carbonatite intrusion of Vuoriyärvi (Kola Peninsula, Russia). A LA-ICP-MS study of apatite. *Lithos* **2005**, *85*, 76–92. [[CrossRef](#)]
14. Decrée, S.; Cawthorn, G.; Deloule, E.; Mercadier, J.; Frimmel, H.; Baele, J.-M. Unravelling the processes controlling the apatite formation in the Phalaborwa Complex (South Africa) based on combined cathodoluminescence, LA-ICPMS and in-situ O and Sr isotope analyses. *Contrib. Mineral. Petrol.* **2020**, *175*, 34. [[CrossRef](#)]
15. Doroshkevich, A.G.; Veksler, I.V.; Klemm, R.; Chromova, E.A.; Izbrodin, A.A. Trace-element composition of minerals and rocks in the Belaya Zima carbonatite complex (Russia): Implications for the mechanisms of magma evolution and carbonatite formation. *Lithos* **2017**, *284–285*, 91–108. [[CrossRef](#)]
16. Ruberti, E.; Enrich, G.E.R.; Azzone, R.G.; Comin-Chiaramonti, P.; de Min, A.; Gomes, C.B. The Banhadao alkaline complex, southeastern Brazil: Source and evolution of potassic SiO₂-undersaturated high-Ca and low-Ca magmatic series. *Mineral. Petrol.* **2012**, *104*, 63–80. [[CrossRef](#)]

17. Chmyz, L.; Arnaud, N.; Biondi, J.C.; Azzone, R.G.; Delphine, B.; Ruberti, E. Ar-Ar ages, Sr-Nd isotope geochemistry, and implications for the origin of the silicate rocks of the Jacupiranga ultramafic-alkaline complex (Brazil). *J. S. Am. Earth Sci.* **2017**, *77*, 286–309. [[CrossRef](#)]
18. Kushiro, I. Si-Al relation in clinopyroxenes from igneous rock. *Am. J. Sci.* **1960**, *258*, 548–554. [[CrossRef](#)]
19. Verhoogen, J. Distribution of titanium between silicates and oxides in igneous rocks. *Am. J. Sci.* **1962**, *260*, 211–220. [[CrossRef](#)]
20. Aoki, K.; Shiba, I. Clinopyroxenes from alkaline rocks of Japan. *Am. Mineral.* **1964**, *49*, 1199–1223.
21. Gibb, F.G.F. The zoned clinopyroxenes of the Shiant Isles sill, Scotland. *J. Petrol.* **1973**, *14*, 203–230. [[CrossRef](#)]
22. Leterrier, J.; Maury, R.C.; Thonon, P.; Girard, D.; Marchal, M. Clinopyroxene composition as a method of identification of the magmatic affinities of paleo-volcanic series. *Earth Planet. Sci. Lett.* **1982**, *59*, 139–154. [[CrossRef](#)]
23. Irving, A.J.; Frey, F.A. Trace element abundances in megacrysts and their host basalts: Constraints on partition coefficients and megacryst genesis. *Geochim. Cosmochim. Acta.* **1984**, *48*, 1201–1221. [[CrossRef](#)]
24. Akinin, V.V.; Sobolev, A.V.; Ntaflos, T.; Richter, W. Clinopyroxene megacrysts from Enmelen melanephelinitic volcanoes (Chukchi Peninsula, Russia): Application to composition and evolution of mantle melts. *Contrib. Mineral. Petrol.* **2005**, *150*, 85–101. [[CrossRef](#)]
25. Harlov, D.E.; Andersson, U.B.; Forster, H.-J. Apatite-monzite relations in the Kiirunavaara magnetite-apatite ore, northern Sweden. *Chem. Geol.* **2002**, *191*, 47–52. [[CrossRef](#)]
26. Lu, J.; Chen, W.; Ying, Y.; Ying, Y.-C.; Jiang, S. Apatite texture and trace element chemistry of carbonatite-related REE deposits in China: Implications for petrogenesis. *Lithos* **2021**, *398–399*, 106276. [[CrossRef](#)]
27. Gittins, J. The origin and evolution of carbonatite magmas. In *Carbonatites Genesis and Evolution*; Bekk, K., Ed.; Unwin Hyman: London, UK, 1989; pp. 580–600.
28. Veksler, I.V.; Nielsen, T.F.D.; Sokolov, S.V. Mineralogy of crystallized melt inclusions from Gardiner and Kovdor ultramafic alkaline complexes: Implications for carbonatite genesis. *J. Petrol.* **1988**, *39*, 2015–2031. [[CrossRef](#)]
29. Stoppa, F.; Rosatelli, G.; Wall, F.; Jeffries, T. Geochemistry of carbonatite-silicate pairs in nature: A case history from Central Italy. *Lithos* **2005**, *85*, 279–281. [[CrossRef](#)]
30. Veksler, I.V.; Dorfman, A.M.; Dulski, P.; Kamenetsky, V.S.; Danyushevsky, L.V.; Jeffries, T.; Dingwel, D. Partitioning of elements between silicate melt and immiscible fluoride, chloride, carbonate, phosphate and sulfate melts, with implications to the origin of natrocarbonatite. *Geochim. Cosmochim. Acta* **2012**, *79*, 20–40. [[CrossRef](#)]
31. Borisova, A.Y.; Tilhac, R. Derivation of Hawaiian rejuvenated magmas from deep carbonated mantle sources: A review of experimental and natural constraints. *Earth Sci. Rev.* **2021**, *222*, 103819. [[CrossRef](#)]
32. Bayanova, T.B. Baddeleyite: A promising geochronometer for alkaline and basic magmatism. *Petrology* **2006**, *14*, 187–200. [[CrossRef](#)]
33. O'Brien, H.; Heilimov, E.; Heino, P. The Archean Siilinjärvi carbonatite complex. In *Mineral Deposits of Finland*; Maier, W.D., Lahtinen, R., O'Brien, H., Eds.; Elsevier: Amsterdam, The Netherlands, 2015; pp. 327–343.
34. Wu, F.J.; Yang, Y.H.; Li, Q.L.; Mitchell, R.H.; Dawson, J.B.; Brandl, G.; Yuhara, M. In situ determination of U-Pb ages and Sr-Nd-Hf isotopic constraints on the petrogenesis of the Phalaborwa carbonatite complex, South Africa. *Lithos* **2011**, *127*, 209–327. [[CrossRef](#)]
35. Gogol, O.; Delinitzin, A. New Rb-Sr data for Kola alkaline province. In *Proceedings of the 10th Kratz Conference*; Kola Science Centre: Apatity, Russia, 1999; pp. 43–47.
36. Yaxley, G.M.; Anenburg, M.; Tappe, S.; Decree, S.; Guzmics, T. Carbonatites: Classification, Sources, Evolution, and Emplacement. *Annu. Rev. Earth Planet. Sci.* **2022**, *50*, 261–293. [[CrossRef](#)]
37. Hawkesworth, C.J.; Cawood, P.A.; Dhuime, B.; Kemp, A.I.S. Earth's continental lithosphere through time. *Annu. Rev. Earth Planet. Sci.* **2017**, *45*, 169–198. [[CrossRef](#)]
38. Belousova, E.A.; Griffin, W.L.; O'Reilly, S.Y.; Fisher, N.I. Apatite as an indicator mineral for mineral exploration: Trace-element compositions and their relationship to host rock type. *J. Geochem. Explor.* **2002**, *76*, 45–69. [[CrossRef](#)]

Disclaimer/Publisher's Note: The statements, opinions and data contained in all publications are solely those of the individual author(s) and contributor(s) and not of MDPI and/or the editor(s). MDPI and/or the editor(s) disclaim responsibility for any injury to people or property resulting from any ideas, methods, instructions or products referred to in the content.